


## Signatures of excited-state quantum phase transitions in quantum many-body systems: Phase space analysis

Qian Wang 

*Department of Physics, Zhejiang Normal University, Jinhua 321004, China  
and CAMTP-Center for Applied Mathematics and Theoretical Physics, University of Maribor, Mladinska 3, SI-2000 Maribor, Slovenia*

Francisco Pérez-Bernal 

*Departamento de Ciencias Integradas y Centro de Estudios Avanzados en Física, Matemáticas y Computación,  
Universidad de Huelva, Huelva 21071, Spain  
and Instituto Carlos I de Física Teórica y Computacional, Universidad de Granada, Granada 18071, Spain*

 (Received 8 May 2021; revised 26 July 2021; accepted 31 August 2021; published 15 September 2021)

Using the Husimi quasiprobability distribution, we investigate the phase space signatures of excited-state quantum phase transitions (ESQPTs) in the Lipkin-Meshkov-Glick and coupled top models. We show that the ESQPT is evinced by the dynamics of the Husimi function, that exhibits a distinct time dependence in the different ESQPT phases. We also discuss how to identify the ESQPT signatures from the long-time averaged Husimi function and its associated marginal distributions. Moreover, from the calculated second moment and Wherl entropy of the long-time averaged Husimi function, we estimate the critical points of the ESQPT in both models, obtaining a good agreement with analytical (mean field) results. We provide a firm evidence that phase space methods are both a new probe for the detection and a valuable tool for the study of ESQPTs.

DOI: [10.1103/PhysRevE.104.034119](https://doi.org/10.1103/PhysRevE.104.034119)

### I. INTRODUCTION

The pioneering works of Weyl [1] and Wigner [2] paved the way to the development of the so-called phase space methods in quantum mechanics [3–8]. In this approach, a quantum state is described by a quasiprobability distribution, defined in classical phase space, instead of by a density matrix in Hilbert space [2,9–13]. Consequently, the expectation value of quantum operators are obtained as average of their classical counterpart over the classical phase space in novel algebraic ways. From this point of view, quantum mechanics is a statistical theory on the classical phase space [14,15]. Phase space methods are specially valued due to the insights into the correspondence between quantum and classical systems they offer [16,17]. As an alternative formulation of quantum mechanics, phase space methods have numerous applications in many areas of physics, e.g., quantum optics [18], atomic physics [19,20], quantum chaos [21,22], condensed matter physics [23,24], and quantum thermodynamics [25–27]. In particular, recent studies have shown that phase space methods are a powerful tool for the understanding of quantum phase transitions in many-body systems [28–35].

Following this path, our aim is to show that excited-state quantum phase transitions (ESQPTs) can be characterized making use of phase space methods. To this end, making use of the Husimi quasiprobability distribution, we analyze the phase space signatures of ESQPTs in two different quantum many-body models. As a generalization of the well-known ground-state quantum phase transition [36], an ESQPT is characterized by the nonanalyticity of the density of states at

certain critical energy value,  $E_c$  [37–39]. ESQPTs have been identified in different quantum systems [40–48]. Moreover, ESQPT's experimental signatures have also been found in various many-body systems [49–53]. Many of these works pay heed to ESQPT effects over nonequilibrium properties of quantum many-body systems [54–64]. Such studies have, in turn, suggested new ways for detecting ESQPTs making use of nonequilibrium quantum dynamics in many-body systems [65–68], paving the way to the access to ESQPTs through current experimental technologies [69]. In addition, the relationship between ESQPTs and the onset of chaos, thermal phase transitions, or exceptional points in non-Hermitian systems have also received a great deal of attention [70–74]. For a recent and complete review on the subject of ESQPTs, see Ref. [75].

In spite of these developments, we still lack a complete understanding of ESQPTs. In the present work, we focus on the phase space signatures of ESQPTs in two well-known quantum many-body systems. Specifically, we use the Husimi quasiprobability function and its associated marginal distributions to characterize the ESQPTs in the Lipkin-Meshkov-Glick (LMG) and coupled top (CT) models. On the one hand, we consider the dynamics of the Husimi function following a sudden quench process and, on the other hand, we focus on the properties of the long-time averaged Husimi function and its marginal distributions. Our main result is the remarkable changes in the time evolved Husimi function once the quench parameter straddles the critical ESQPT energy. Therefore, an ESQPT can be clearly identified by the dynamics of the Husimi function. This is further reflected

in sharp changes in the long-time averaged Husimi function and its marginal distributions due to the ESQPT. In addition to these two main issues, we also discuss how to estimate the ESQPT critical energy using the second moment and the Wehrl entropy of the long-time averaged Husimi function, obtaining a fine agreement between numerical and analytical results. Hence, from our analysis it can be deduced that phase space methods are a useful and convenient tool for the study of ESQPTs.

The article is organized as follows. In Sec. II, we introduce the Husimi function and its marginal distributions, as well as the definitions of their second moment and Wehrl entropy. In Sec. III, we present, respectively, the Hamiltonians of the LMG and CT models together with a brief outline of their basic features, mainly focusing on their associated ESQPTs and in Sec. IV we report the obtained results for both models. Finally, we summarize our results together with some concluding remarks in Sec. V.

## II. HUSIMI FUNCTION

As the Gaussian smoothing of the Wigner function, the Husimi quasiprobability distribution, also known as  $Q$  function, is a positive-definite function defined as follows [7,9,76]:

$$Q(p, q) = \langle \zeta(p, q) | \rho | \zeta(p, q) \rangle, \quad (1)$$

where  $\rho = |\psi\rangle\langle\psi|$  is a quantum state of the system under study and  $|\zeta(p, q)\rangle$  denotes a minimal uncertainty (coherent) state centered in the phase space point  $(p, q)$ , with  $p$  and  $q$  the canonical momentum and position, respectively. From the well-known fact that a coherent state  $|\zeta(p, q)\rangle$  covers a phase space region centered at  $(p, q)$  with volume  $\hbar$ , the Husimi function can be considered as the probability of observing the system in that phase space region [77]. Hereafter, for simplicity's sake, we set  $\hbar = 1$ .

For spin systems, such as the ones studied in this work, the Husimi function can be calculated by using the so-called SU(2) spin- $j$  coherent states (Bloch states) [78,79]

$$|\zeta\rangle = (1 + |\zeta|^2)^{-j} e^{\zeta \hat{J}_+} |j, -j\rangle, \quad (2)$$

where  $\zeta \in \mathbb{C}$ ,  $\hat{J}_+ = \hat{J}_x + i\hat{J}_y$  is the spin raising operator, and  $|j, -j\rangle$  is the eigenstate of  $\hat{J}_z$  with eigenvalue  $-j$ , that is,  $\hat{J}_z |j, -j\rangle = -j |j, -j\rangle$ , and  $\hat{J}_{\{x,y,z\}}$  are the components of the spin angular momentum operator. The set of coherent states is an overcomplete set—this is the reason why the Husimi function is a quasiprobability distribution instead of a probability distribution—and it satisfies the closure relation

$$\frac{2j+1}{\pi} \int_{\mathbb{R}^2} |\zeta\rangle\langle\zeta| \frac{d^2\zeta}{(1+|\zeta|^2)^2} = \mathbf{1}, \quad (3)$$

where  $d^2\zeta = d\text{Re}(\zeta)d\text{Im}(\zeta)$  is the integration measure on  $\mathbb{C}$ . To visualize the Husimi function in phase space  $(p, q)$ , we parametrize  $\zeta$  in terms of the canonical variables  $q$  and  $p$  as [63,80]

$$\zeta(p, q) = \frac{q - ip}{\sqrt{4 - (p^2 + q^2)}}, \quad (4)$$

with  $p^2 + q^2 \leq 4$ . Then it is straightforward that the closure relation in phase space Eq. (3) can be rewritten as

$$\frac{2j+1}{4\pi} \int_{\Omega} |\zeta(p, q)\rangle\langle\zeta(p, q)| dpdq = \mathbf{1}, \quad (5)$$

where the integration area  $\Omega$  is defined by  $p^2 + q^2 \leq 4$ . Hence, the normalization condition of the Husimi function Eq. (1) in phase space is given by

$$\frac{2j+1}{4\pi} \int_{\Omega} Q(p, q) dpdq = 1. \quad (6)$$

Many features of a system can be derived from the moments of the Husimi function [23,28–31,76,81]. Among all moments, an important and very useful one is the second moment (also known as the generalized inverse participation ratio), which quantifies the degree of localization of a quantum state in phase space, and read as

$$M_2 = \frac{2j+1}{4\pi} \int_{\Omega} Q^2(p, q) dpdq. \quad (7)$$

In the case of an extremely extended state,  $\rho = |\psi\rangle\langle\psi|$ , the phase space would be uniformly covered and  $Q(p, q) \sim 1/(2j+1)$ . In this case, one can find that  $M_2 \sim 1/(2j+1)$  which tends to zero as  $j \rightarrow \infty$ . Hence, the smaller is the value of  $M_2$ , the higher is the degree of delocalization of state  $|\psi\rangle$  in phase space. However, if the state  $\rho = |\psi\rangle\langle\psi|$  is concentrated in one phase space point  $(p_0, q_0)$ , then we expect  $Q(p, q) \sim \exp[-(q - q_0)^2/(2\sigma_q^2) + (p - p_0)^2/(2\sigma_p^2)]$ , in accordance with the normalization condition,  $\sigma_q\sigma_p = 2/(2j+1)$ . In the classical limit  $j \rightarrow \infty$ , one can see in this second case,  $Q(p, q)$  shrinks to the point  $(p_0, q_0)$ , as expected and the second moment of Husimi function for this maximally localized state is  $M_2 \sim 1/2$ . Therefore,  $M_2 \in [0, 1/2]$  with the maximum value associated with a maximum localization state in phase space.

Besides the second moment of the Husimi function, another quantity that has been employed in various studies to characterize the properties of the Husimi function is the Wehrl entropy [28–32,82]. As the classical counterpart of the quantum von Neumann entropy, the Wehrl entropy is defined as [83]

$$W = -\frac{2j+1}{4\pi} \int_{\Omega} Q(p, q) \ln[Q(p, q)] dpdq. \quad (8)$$

Here, it is worth pointing out that the second moment  $M_2$  in Eq. (7) can be considered as a linearized version of the Wehrl entropy. Therefore, the Wehrl entropy also provides a measurement of the degree of localization of a quantum state in phase space. However, in contrast with  $M_2$ , the degree of delocalization increases for increasing  $W$  values. For the fully extended states, we have  $W_{\max} \sim \ln(2j+1)$ . In addition to this, the Lieb conjecture shows that the minimum Wehrl entropy is  $W_{\min} = j/(j+1)$ , so that  $W_{\min} \rightarrow 1$  as  $j \rightarrow \infty$  [84].

It is worth emphasizing that both localization measures,  $M_2$  and  $W$ , are related to the Rényi-Wehrl entropy, defined as [85]

$$S_{\alpha} = \frac{1}{1-\alpha} \left\{ \ln \left[ \frac{2j+1}{4\pi} \int_{\Omega} dpdq Q^{\alpha}(p, q) \right] \right\}, \quad (9)$$

where  $Q(p, q)$  is the Husimi function Eq. (1) and  $\alpha \geq 0$  is the Rényi index. It has been shown that the exponential of  $S_\alpha$  acts as a useful indicator of the degree of localization of the system in phase space, from which the Rényi volume of order  $\alpha$  term has been coined [86]. In our work, we can see that  $S_\alpha$  tends to  $W$  as  $\alpha \rightarrow 1$ , while  $M_2 = \exp(-S_2)$ .

An extra insight into the phase space features of a quantum state can be obtained from the marginal distributions of the Husimi function in position and momentum space, respectively. For a spin- $j$  coherent state, they are defined as

$$\begin{aligned} Q(q) &= \sqrt{\frac{2j+1}{4\pi}} \int Q(p, q) dp, \\ Q(p) &= \sqrt{\frac{2j+1}{4\pi}} \int Q(p, q) dq, \end{aligned} \quad (10)$$

with a normalization condition

$$\sqrt{\frac{2j+1}{4\pi}} \int Q(q) dq = \sqrt{\frac{2j+1}{4\pi}} \int Q(p) dp = 1. \quad (11)$$

Accordingly, the second moment and the Wehrl entropy of the marginal distributions are defined as

$$\begin{aligned} M_2^{(\mu)} &= \sqrt{\frac{2j+1}{4\pi}} \int Q^2(\mu) d\mu, \\ W^{(\mu)} &= -\sqrt{\frac{2j+1}{4\pi}} \int Q(\mu) \ln[Q(\mu)] d\mu, \end{aligned} \quad (12)$$

where  $\mu = p, q$ .

The marginal distributions  $Q(q)$  and  $Q(p)$  of the Husimi function are not equal to the density functions  $|\langle q|\psi\rangle|^2$  and  $|\langle p|\psi\rangle|^2$ , in sharp contrast to what happens in the case of the Wigner distribution. In fact, they are Gaussian smeared density distributions in position and momentum spaces, respectively [28,87]. Note further that, in general,  $|M_2 - M_2^{(p)} M_2^{(q)}| = \delta M_2 \neq 0$  and  $|W - [W^{(p)} + W^{(q)}]| = \delta W \neq 0$ , where  $\delta M_2$  and  $\delta W$  decrease as the system size increases except in the vicinities of some singular points, e.g., quantum critical points [23,28,87].

We proceed now explaining the main features of the LMG and CT models to continue exploiting the properties of the Husimi function given above to explore the ESQPT signatures in both models.

### III. MODELS

#### A. Lipkin-Meshkov-Glick model

The Lipkin-Meshkov-Glick (LMG) model describes  $N$  spin-1/2 particles interacting through infinite range interactions plus an external magnetic field. It was first introduced as a toy model, to explore phase transitions in nuclear systems [88] and, since then, it has been exploited as a paradigmatic model in the study of quantum phase transitions [89–94]. As the LMG model has broad applications in different fields of physics, it has attracted a great deal of attention from both a theoretical [95–98] and an experimental [99–104] perspective in recent years.

By using collective operators  $\hat{J}_\alpha = \sum_k^N \hat{\sigma}_k^\alpha / 2$ ,  $\{\alpha = x, y, z\}$  where  $\hat{\sigma}_k^\alpha$  is the  $\alpha$ th component of the  $k$ th spin Pauli matrix,

the LMG model Hamiltonian can be written as

$$\hat{H}_{\text{LMG}} = -\frac{4(1-\kappa)}{N} \hat{J}_x^2 + \kappa \left( \hat{J}_z + \frac{N}{2} \right), \quad (13)$$

where  $\kappa$  denotes the strength of the external magnetic field. The total spin operator  $\hat{\mathbf{J}}^2 = \hat{\mathbf{J}}_x^2 + \hat{\mathbf{J}}_y^2 + \hat{\mathbf{J}}_z^2$  with eigenvalue  $j(j+1)$  commutes with the Hamiltonian and, therefore,  $j$  is a constant of the motion. In our study, we select the spin sector with  $j = N/2$ , with a dimension of the Hamiltonian matrix equal to  $\mathcal{D}_{\text{LMG}} = N + 1$ . Moreover, the Hamiltonian also commutes with the parity operator  $\hat{\Pi}_{\text{LMG}} = e^{i\pi(j+m)}$ , where  $m \in \{-j, -j+1, \dots, j\}$  is the eigenvalue of  $\hat{J}_z$ . Therefore, the Hamiltonian matrix is further split into even- and odd-parity blocks, with dimensions  $\mathcal{D}_{\text{LMG}}^e = N/2 + 1$  and  $\mathcal{D}_{\text{LMG}}^o = N/2$ , respectively. We focus on the even-parity block, which includes the ground state of the system.

The LMG model undergoes a second-order ground-state quantum phase transition from the paramagnetic phase with  $\kappa < \kappa_c$  to the ferromagnetic phase with  $\kappa > \kappa_c$  at the critical point  $\kappa_c = 4/5$  [91–93]. The ground-state quantum phase transition of the Lipkin model has been studied extensively in numerous works [91–96,105,106]. In particular, the ground-state quantum phase transition of the LMG model has been explored using the Husimi quasiprobability distribution in Ref. [30]. Our aim is to analyze, using the Husimi function, the signatures of the ESQPT of the LMG model in phase space. Such ESQPT happens at a critical energy  $E_c = 0$  for control parameter values  $\kappa < \kappa_c$  [38,55], and it is evinced by the singular behavior of the density of states  $\omega_{\text{LMG}}(E) = \sum_n \delta(E - E_n)$  at the critical energy.

In Fig. 1(a), we plot the correlation energy diagram of the LMG model with  $j = N/2 = 20$  as a function of  $\kappa$ . We can see that energy levels exhibit an obvious collapse around  $E_c = 0$  for  $\kappa < \kappa_c$ . This explains the appearance of a sharp density of states peak in the neighborhood of  $E_c = 0$ . Indeed, as can be seen from Fig. 1(b), both numerical and semiclassical results [55] show that, at the critical energy  $E_c = 0$ ,  $\omega_{\text{LMG}}(E)$  displays a cusp-type singularity which turns into a logarithmic divergence as  $j = N/2 \rightarrow \infty$  [39,89].

#### B. Coupled top model

The second model considered is the coupled top (CT) model, also known as the Feingold-Peres model [107–111]. It describes the interaction between two large spins whose respective angular momentum operators are  $\hat{\mathbf{J}}_1 = (\hat{J}_{1x}, \hat{J}_{1y}, \hat{J}_{1z})$  and  $\hat{\mathbf{J}}_2 = (\hat{J}_{2x}, \hat{J}_{2y}, \hat{J}_{2z})$ , and the Hamiltonian takes the form

$$\hat{H}_{\text{CT}} = \hat{J}_{1z} + \hat{J}_{2z} + \frac{\xi}{j} \hat{J}_{1x} \hat{J}_{2x}, \quad (14)$$

where  $\xi$  is the coupling strength between both spins. Hereafter, we assume that the two spins have identical magnitude, therefore the eigenvalues of  $\hat{\mathbf{J}}_1^2$  and  $\hat{\mathbf{J}}_2^2$  are  $j(j+1)$ . In this case, the dimension of the Hilbert space is  $\mathcal{D}_{\text{HCT}} = (2j+1)^2$ . However, as the Hamiltonian in Eq. (14) remains invariant under the permutation of the two spins ( $\hat{\mathcal{P}}$ ) and under parity  $\hat{\Pi}_{\text{CT}} = e^{i\pi(2j+m_1+m_2)}$ , where  $m_1, m_2 \in \{-j, -j+1, \dots, j\}$  are the eigenvalues of  $\hat{J}_{1z}$  and  $\hat{J}_{2z}$ , the Hilbert space can be further decomposed into four subspaces according to the eigenvalues of  $\hat{\mathcal{P}}$  and  $\hat{\Pi}_{\text{CT}}$ . On what follows, we focus

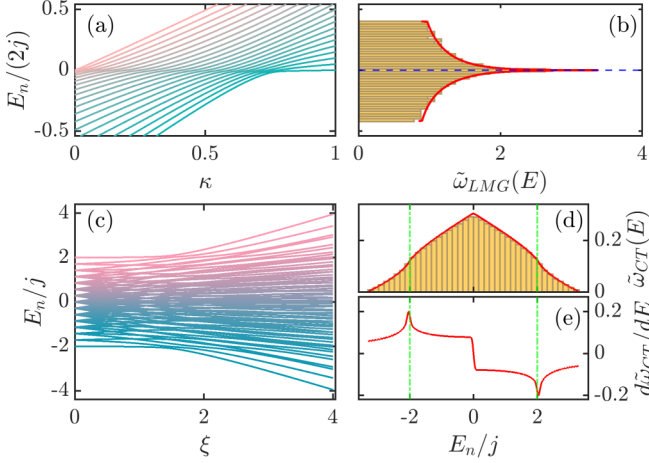


FIG. 1. (a) Energy spectrum (arbitrary units) of the LMG model as a function of  $\kappa$  with  $j = N/2 = 20$ . (b) Rescaled density of states,  $\tilde{\omega}_{\text{LMG}}(E) = \omega_{\text{LMG}}(E)/j$ , for the LMG model with  $\kappa = 0.4$  and  $j = N/2 = 500$ . The red solid line is the semiclassical result and the horizontal blue dashed line denotes the critical energy  $E/(2j) = E_c/(2j) = 0$ . (c) Energy spectrum (arbitrary units) of the CT model as a function of  $\xi$  with  $j = 7$ . (d) Rescaled density of states,  $\tilde{\omega}_{\text{CT}}(E) = \omega_{\text{CT}}(E)/j^2$ , of the CT model with  $\xi = 3$  and  $j = 70$ . The red solid line denotes the semiclassical result. (e) Derivative of  $\tilde{\omega}_{\text{CT}}(E)$  for the CT model with  $\xi = 3$  and  $j = 70$ . Two vertical green dot-dashed lines in panels (d) and (e) indicate the critical energy values  $E/j = E_c/j = \pm 2$  for the ESQPTs in the CT model. The axes in all panels are dimensionless.

on the subspace identified by  $\mathcal{P} = +1$ ,  $\Pi_{\text{CT}} = +1$ , denoted by  $V_{++}$ , which includes the system ground state. We also restrict to integer  $j$  values, thus the dimension of  $V_{++}$  is  $D_{V_{++}} = (j+1)^2$  [110].

The CT model has been studied extensively in diverse fields of physics [109–113]. It is known that its ground state displays a second-order quantum phase transition at a critical control parameter value  $\xi_c = 1$ , which separates a ferromagnetic phase ( $\xi < \xi_c$ ) from a paramagnetic phase ( $\xi > \xi_c$ ) [109,111]. In addition to this, it has been found that the CT model undergoes an ESQPT at critical energies  $E_c/j = \pm 2$  for  $\xi > \xi_c = 1$ . This ESQPT differs from the one in the LMG model; the ESQPTs in the CT model are identified by a non-analyticity in the first derivative of the density of states at the critical energies. This can be explained due to the fact that the number of effective degrees of freedom in this model is  $f = 2$  and, for a nondegenerate critical point, the nonanalyticity is expected to appear in the  $f - 1$ th derivative of the energy level density [43,75]. The difference between this case and the LMG case ( $f = 1$ ) is obvious comparing the LMG and CT density of states in Figs. 1(b) and 1(d).

The correlation energy diagram for the CT model, depicting the energy as a function of control parameter  $\xi$ , is plotted in Fig. 1(c) for  $j = 7$ . It can be easily appreciated how the energy spectrum becomes more complex as the value of  $\xi$  increases. However, as explained above, in this case the energy levels do not pile up around the critical energy as in the LMG model [cf. Fig. 1(a)]. The density of states of the CT model, denoted by  $\omega_{\text{CT}}(E)$ , is a continuous function of energy for  $\xi > \xi_c$ , as shown in Fig. 1(d) for numerical and semi-

classical results [111]. As expected, the CT model ESQPTs are evinced through the singular behavior of the first derivative of  $\omega_{\text{CT}}(E)$ . In Fig. 1(e), we plot the first derivative of  $\tilde{\omega}_{\text{CT}}(E) = \omega_{\text{CT}}(E)/j^2$  as a function of  $E_n/j$  with  $j = 70$ . As it can be seen,  $d\tilde{\omega}_{\text{CT}}(E)/dE$  develops a cusp-type singularity at the critical energy values. Both singularities are expected to become logarithmic divergences in the thermodynamic limit,  $j \rightarrow \infty$  [39,43]. In the following, we will only consider the critical energy values  $E_c/j = -2$ , as the obtained results can be trivially extended to the  $E_c/j = 2$  case.

## IV. RESULTS AND DISCUSSIONS

In this section, we discuss how to identify the signatures of ESQPT from the perspective of quantum phase space by means of the Husimi function in the two aforementioned models. We consider the impact of the ESQPT on the dynamical features of the Husimi function, using a quantum quench protocol and paying heed to the properties of the long-time averaged Husimi function.

### A. Husimi function of the LMG model

In the LMG model case, the quantum quench protocol starts with the model initially prepared in the ground state,  $|\psi_0\rangle$ , of Hamiltonian  $\hat{H}_{\text{LMG}}$  with  $0 < \kappa < \kappa_c$ . At  $t = 0^+$ , we suddenly add an external magnetic field along  $z$  direction with strength  $\eta$ , and let the model evolve under the Hamiltonian  $\hat{H}_{\text{LMG}}^f = \hat{H}_{\text{LMG}} + \eta(\hat{J}_z + N/2)$ . This procedure is akin to the transfer of energy onto the system, leading to a final rescaled quenched energy  $\mathcal{E}_{\text{LMG}}(\kappa, \eta) = \langle \psi_0 | \hat{H}_{\text{LMG}}^f | \psi_0 \rangle / j$ . Obviously,  $\mathcal{E}_{\text{LMG}}(\kappa, \eta)$  depends on both the  $\kappa$  and  $\eta$  values. Eventually, for a fixed  $\kappa$  value, there exists a particular value of  $\eta$  which takes  $\mathcal{E}_{\text{LMG}}(\kappa, \eta)$  to the critical energy of ESQPT in the LMG model [56]. Therefore, we define the  $\eta$  parameter value which leads the system to the critical energy as the critical quench strength,  $\eta_c$ , whose value, obtained through the semiclassical (or coherent state) approach (see Appendices A and B for more details), is given by [54–56]

$$\eta_c = 2 - \frac{5}{2}\kappa, \quad (15)$$

with  $0 < \kappa < \kappa_c$ . We stress that the critical strength  $\eta_c$  to bring the system to the ESQPT critical energy is less than the quench strength which drive the model through the ground-state quantum phase transition [55]. The ESQPT phase diagram in the LMG model is depicted in Fig. 2. At a given  $\kappa$  value, by varying the parameter  $\eta$ , we can access energy values,  $\mathcal{E}_{\text{LMG}}(\kappa, \eta)$ , below, at, and above the critical energy. This means that, depending on the quench strength, the system will explore the different ESQPT phases.

The time dependence of the quantum state is given by  $\rho(t) = |\psi(t)\rangle\langle\psi(t)| = e^{-i\hat{H}_{\text{LMG}}^f t} \rho(0) e^{i\hat{H}_{\text{LMG}}^f t}$  with  $\rho(0) = |\psi_0\rangle\langle\psi_0|$ . Hence, the Husimi function at time  $t$  can be written as

$$Q_t(p, q) = \langle \zeta(p, q) | \rho(t) | \zeta(p, q) \rangle \\ = \left| \sum_n e^{-iE_n t} \langle \zeta(p, q) | E_n \rangle \langle E_n | \psi_0 \rangle \right|^2, \quad (16)$$

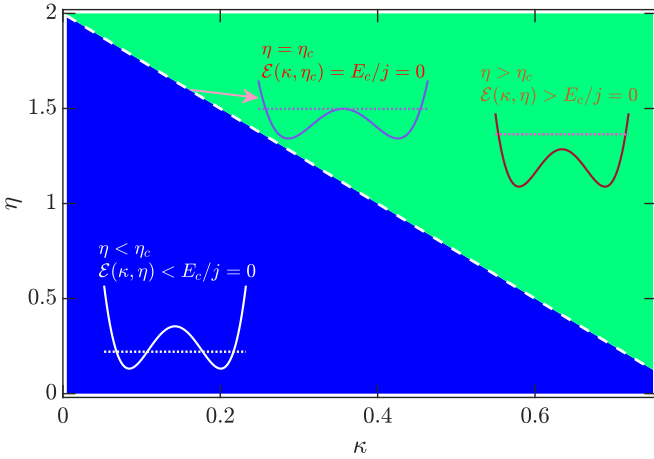


FIG. 2. Schematic demonstration of the LMG model excited state phase diagram. The system is initialized in the  $\hat{H}_{\text{LMG}}$  model ground state with  $0 < \kappa < 4/5$ , and an external magnetic field along the  $z$  axis with  $\eta$  strength is suddenly applied to the model. This sudden quantum quench process gives rise to two different phases, separated by the critical line  $\eta_c = 2 - 5\kappa/2$ , plotted with a white dashed line: For  $\eta < \eta_c$  ( $\eta > \eta_c$ ), the quenched system energy is less (greater) than the critical ESQPT energy,  $\mathcal{E}_{\text{LMG}}(\kappa, \eta) < E_c/j = 0$  [ $\mathcal{E}_{\text{LMG}}(\kappa, \eta) > E_c/j = 0$ ]. The quenched system energy equals the ESQPT critical energy along the critical line. In addition, two phases are also manifested in the classical dynamics of a particle in a double-well potential, which exhibits either a localized ( $\eta < \eta_c$ ) or a delocalized ( $\eta > \eta_c$ ) behavior. Further details are given in the main text and the Appendices B and C. The axes in the figure are dimensionless.

where  $|E_n\rangle$  is the  $n$ th eigenstate of  $\hat{H}_{\text{LMG}}^f$  with eigenvalue  $E_n$ . Thus,  $Q_t(p, q)$  is strongly dependent on the overlaps between the initial state and the  $\hat{H}_{\text{LMG}}^f$  eigenstates.

In Fig. 3, we plot the Husimi function of the LMG model at different time steps for several values of  $\eta$ , with  $\kappa = 0.4$  and  $N = 400$ . The critical quench strength given by Eq. (15) is  $\eta_c = 1$  in this case. We first note that the ground state in the even-parity sector can be correctly described by the so-called even coherent states [30,93,114],  $|\zeta(p, q)\rangle_+ = \mathcal{N}_+(p, q)[|\zeta(p, q)\rangle + |\zeta(-p, -q)\rangle]$ , where  $\mathcal{N}_+(p, q) = 1/\sqrt{2}\{1 + [1 - (p^2 + q^2)/2]^{2j}\}$  is a normalization constant. As a result, the Husimi function of the initial state is represented by two symmetrically-localized wave packets in phase space, as seen in the first column of Fig. 3. As time passes, the Husimi function behavior is qualitatively different depending on the  $\eta$  value being below, at, or above the critical value  $\eta_c = 1$ . Specifically, as can be observed in the top row of Fig. 3, the Husimi function displays two distinct localized wave packets in its time evolution for  $\eta < \eta_c$ . At the critical point  $\eta = \eta_c$  [shown in the panels of the second row in Fig. 3], the evolution of the Husimi function implies a larger extension of phase space than in the previous case and, in particular, the initially disconnected maxima are fused in a single maximum. Finally, in the  $\eta > \eta_c$  case, the two initially separated wave packets again merge into a single one with a zero value in the origin, as illustrated in the last row of Fig. 3. The strikingly distinct behaviors in the dynamics of Husimi function on both sides of the ESQPT suggests that the underlying transition has nontrivial impacts on the model dynamics. Moreover, the particular dynamical behavior of the Husimi function at  $\eta = \eta_c$  may be used as a probe to test the occurrence of an ESQPT.

The different features observed in Fig. 3 can be understood from the dynamics of a classical counterpart of the LMG model. As shown in the insets of Fig. 2, in a semiclassical approach the LMG model Hamiltonian for the parameter range  $0 < \kappa < \kappa_c$  can be described as a classical particle confined within a double well potential (an explicit derivation of this

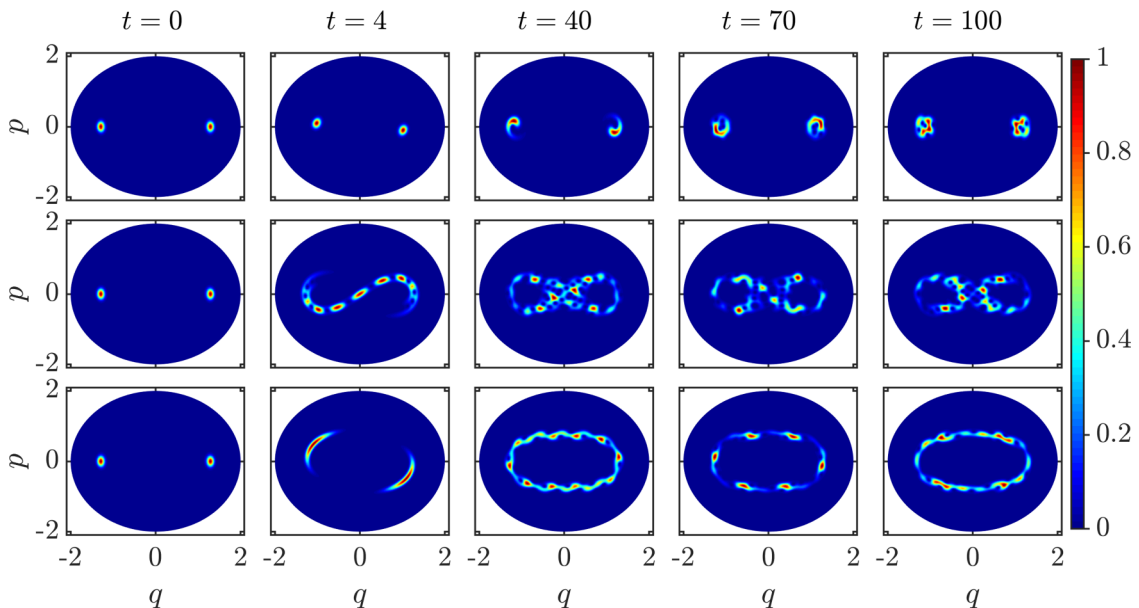


FIG. 3. Snapshots of the rescaled spin Husimi function  $\mathcal{Q}_t(p, q) = Q_t(p, q)/Q_t^m$ , with  $Q_t^m$  being the maximum value of  $Q_t(p, q)$ , at different time steps for the LMG model with  $\eta = 0.4, 1, 1.7$  (from top to bottom). All panels:  $j = N/2 = 200$  and  $\kappa = 0.4$ . The axes in all panels are dimensionless.

point is provided in Appendix C). In this case, the initial state, being the system ground state, is initially located at the points corresponding to the potential minima. The sudden quench of  $\eta$  leads to the particle gaining an energy  $\mathcal{E}_{\text{LMG}}(\kappa, \eta)$ . Hence, the particle dynamics is governed by the energy difference between  $\mathcal{E}_{\text{LMG}}(\kappa, \eta)$  and the relative height of the central barrier, which is equal to the critical ESQPT energy. For  $\eta < \eta_c$ ,  $\mathcal{E}(\kappa, \eta) < E_c/j = 0$ , and the particle, without enough energy to go through the central barrier, is kept confined within the wells. In this case, the classical dynamics in phase space consists of two disconnected and localized regions. On the contrary, for  $\eta > \eta_c$ ,  $\mathcal{E}(\kappa, \eta) > E_c/j$ , and the particle is able to straddle both wells freely. Thus, the two previously disconnected regions of the phase space merge into a single, delocalized, one. At  $\eta = \eta_c$ , the quenched energy and the critical energy are equal. In this case, the particle classically could be as close as possible to the top of the central barrier and, as a consequence, the disconnected regions at  $\eta < \eta_c$  start to fuse. Further details on the classical dynamics and phase space structures of the LMG model are provided in Appendix C.

Additional ESQPT signatures can be revealed through the long-time averaged Husimi function

$$\bar{Q}(p, q) = \langle \zeta(p, q) | \bar{\rho} | \zeta(p, q) \rangle, \quad (17)$$

where  $\bar{\rho}$  is the long-time averaged state of the model, defined as

$$\bar{\rho} = \lim_{T \rightarrow \infty} \frac{1}{T} \int_0^T \rho(t) dt. \quad (18)$$

For the LMG model, it is straightforward that the explicit expression of the long-time averaged Husimi function is

$$\bar{Q}_{\text{LMG}}(p, q) = \sum_n |\langle \zeta(p, q) | E_n \rangle|^2 |\langle E_n | \psi_0 \rangle|^2. \quad (19)$$

Again, the overlap between the initial state,  $|\psi_0\rangle$ , and the  $n$ th eigenstate of  $H_{\text{LMG}}^f$  plays a crucial role in determining the long-time averaged values  $\bar{Q}_{\text{LMG}}(p, q)$ .

In the upper panels of Fig. 4, we depict  $\bar{Q}_{\text{LMG}}(p, q)$  for three different values of  $\eta$ : one below the critical value [ $\eta = 0.4$ , Fig. 4(a)], for the critical value [ $\eta_c = 1$ , Fig. 4(b)], and one above the critical value [ $\eta = 1.8$ , Fig. 4(c)]. The structure of  $\bar{Q}_{\text{LMG}}(p, q)$  changes drastically as  $\eta$  goes through the critical point. For  $\eta < \eta_c$ ,  $\bar{Q}_{\text{LMG}}(p, q)$  consists of two localized and disconnected parts. As  $\eta$  increases, the surface of the two disconnected parts increases and they join once  $\eta = \eta_c = 1$ . If the  $\eta$  value increases beyond  $\eta_c$ , then the two parts are merged into a single one. It is worth to emphasize that  $\bar{Q}_{\text{LMG}}(p, q)$  has a rather larger degree of delocalization at  $\eta = \eta_c$ . The features of  $\bar{Q}_{\text{LMG}}(p, q)$  are more visible in its marginal distributions,  $\bar{Q}_{\text{LMG}}(q)$  and  $\bar{Q}_{\text{LMG}}(p)$  [cf. Eq. (10)]. Both are plotted for several values of  $\eta$ , in Figs. 4(d) and 4(e), where it is made clear how the width of  $\bar{Q}_{\text{LMG}}(q)$  and  $\bar{Q}_{\text{LMG}}(p)$  increases for increasing  $\eta$  values, in good agreement with the extension of  $\bar{Q}_{\text{LMG}}(p, q)$  in phase space shown in the upper panels of the same figure. Moreover, the particular shape of the marginal distributions at  $\eta_c = 1$  evidences that these quantities, and in particular  $\bar{Q}_{\text{LMG}}(q)$ , may be valid ESQPT indicators. Here, we should point out that the long-time averaged Husimi function

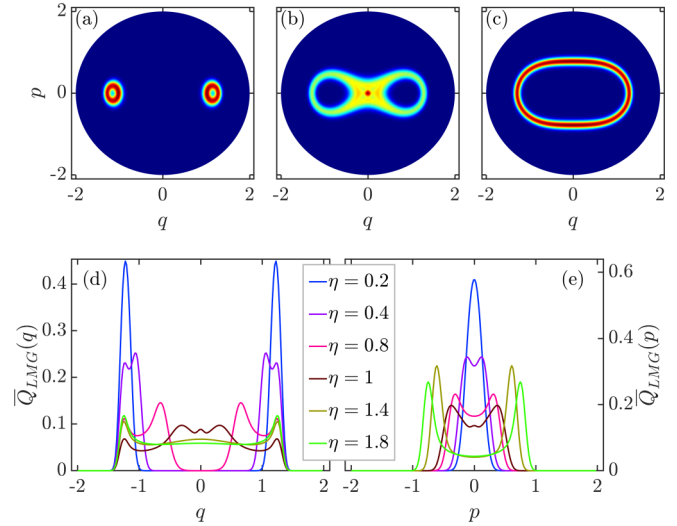


FIG. 4. Rescaled long-time averaged Husimi function  $\bar{Q}_{\text{LMG}}(p, q) = \bar{Q}_{\text{LMG}}(p, q) / \bar{Q}_{\text{LMG},m}$  of the LMG model for (a)  $\eta = 0.4$ , (b)  $\eta = 1$ , and (c)  $\eta = 1.8$  with  $j = N/2 = 200$  and  $\kappa = 0.4$ . Here  $\bar{Q}_{\text{LMG},m}$  denotes the maximum value of  $\bar{Q}_{\text{LMG}}(p, q)$ . Marginal distributions of  $\bar{Q}_{\text{LMG}}(p, q)$ ,  $\bar{Q}_{\text{LMG}}(q)$ , and  $\bar{Q}_{\text{LMG}}(p)$ , for several values of  $\eta$  are plotted in panels (d) and (e), respectively. All quantities are unitless.

provides the skeleton of the evolved Husimi function, such as the long-time averaged Wigner function does [115].

To further elucidate the ESQPT signatures in the properties of  $\bar{Q}_{\text{LMG}}(p, q)$ , we evaluate the second moment of this quantity,  $\bar{M}_{2,\text{LMG}}$  [see Eq. (7)], and the Wehrl entropy,  $\bar{W}_{\text{LMG}}$  [see Eqs. (8)]. In Figs. 5(a) and 5(b),  $\bar{M}_{2,\text{LMG}}$  and  $\bar{W}_{\text{LMG}}$  are depicted as a function of  $\eta$  for several  $\kappa$  values. Both the second moment and the Wehrl entropy reach extremal values (minimum and maximum, respectively) at the corresponding critical  $\eta_c$  value. This indicates that once the quenched system reaches the critical ESQPT energy the extension of the resulting quantum state is maximal. Moreover, the extrema in the second moment and Wehrl entropy, denoted as  $\bar{M}_{2,\text{LMG}}^c$  and  $\bar{W}_{\text{LMG}}^c$ , increase for increasing system size values,  $N$ . In the insets of Figs. 5(a) and 5(b), we show how  $\bar{M}_{2,\text{LMG}}^c$  and  $\bar{W}_{\text{LMG}}^c$  vary with  $N$  for several values of  $\eta_c$ .

We find that  $\bar{M}_{2,\text{LMG}}^c$  follows a power-law scaling  $\bar{M}_{2,\text{LMG}}^c \sim N^{-\gamma_M}$ , regardless of the value of  $\eta_c$ . However, in all cases,  $\bar{W}_{\text{LMG}}^c$  exhibits a logarithmic scaling of the form  $\bar{W}_{\text{LMG}}^c \sim \gamma_W \ln(N)$ .

The values of the scaling exponents  $\gamma_M$  and  $\gamma_W$  are depicted in Fig. 5(c) as a function of the  $\eta_c$  value, making clear how  $\gamma_M$  and  $\gamma_W$  decrease for raising  $\eta_c$  values. Therefore, the position of the  $\bar{M}_{2,\text{LMG}}$  and  $\bar{W}_{\text{LMG}}$  extrema are valid candidates for the estimation of the ESQPT critical point. To check this, we compare the numerically obtained critical points with the analytical ones from Eq. (15). We obtain a fine agreement between both approaches, as can be observed in Fig. 5(d). These results suggest that the  $\bar{Q}_{\text{LMG}}(p, q)$  second moment and Wehrl entropy are reliable probes able to detect the ESQPT in the LMG model.

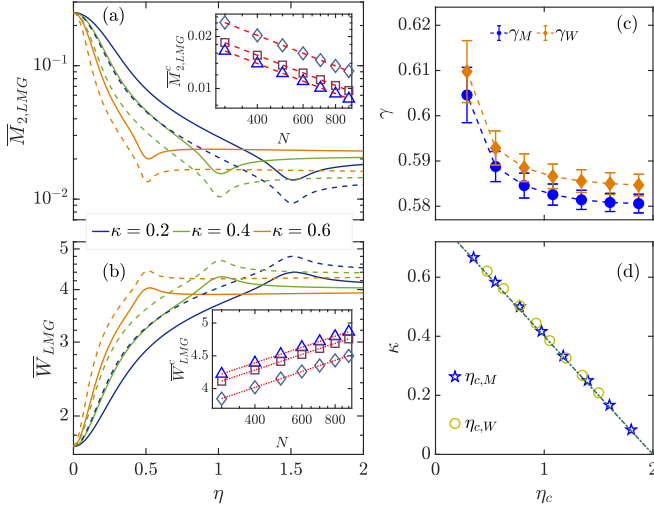


FIG. 5. (a) Second moment of  $\overline{Q}_{\text{LMG}}(p, q)$  as a function of  $\eta$  for several  $\kappa$  with  $j = N/2 = 200$  (solid lines) and  $j = N/2 = 400$  (dashed lines). Inset: Critical second moment,  $\overline{M}_{2,\text{LMG}}^c = \overline{M}_{2,\text{LMG}}(\eta_c)$ , as a function of  $N$  for  $\eta_c = 1.5$  (triangles),  $\eta_c = 1$  (squares), and  $\eta_c = 0.5$  (diamonds). Red dashed lines are of the form  $\overline{M}_{2,\text{LMG}}^c \sim N^{-\gamma_M}$ . (b) Wehrl entropy of  $\overline{Q}_{\text{LMG}}(p, q)$  as a function of  $\eta$  for various  $\kappa$  with  $j = N/2 = 200$  (solid lines) and  $j = N/2 = 400$  (dashed lines). Inset: Critical Wehrl entropy,  $\overline{W}_{\text{LMG}}^c = \overline{W}_{\text{LMG}}(\eta_c)$ , as a function of  $N$  for  $\eta_c = 1.5$  (triangles),  $\eta_c = 1$  (squares), and  $\eta_c = 0.5$  (diamonds). Red dotted lines are of the form  $\overline{W}_{\text{LMG}}^c \sim \gamma_W \ln(N)$ . (c) Values of the finite-size scaling exponents of  $\overline{M}_{2,\text{LMG}}$  and  $\overline{W}_{\text{LMG}}$  for several  $\eta_c$  with  $j = N/2 = 200$ . (d) Critical values  $\eta_{c,M}$ ,  $\eta_{c,W}$  estimated from the extrema of  $\overline{M}_{2,\text{LMG}}$  and  $\overline{W}_{\text{LMG}}$ , respectively, for different values of  $\kappa$  with  $j = N/2 = 400$ . The dot-dashed is the analytical result from Eq. (15). The axes in all figures are dimensionless.

For the sake of completeness, we also study the dependence with  $\eta$  of the second moment and Wehrl's entropy of the long-time averaged marginal distributions,  $\overline{Q}_{\text{LMG}}(q)$  and  $\overline{Q}_{\text{LMG}}(p)$ , for several values  $\kappa$ . The obtained results are shown in Fig. 6, where it can be appreciated how the ESQPT induces a remarkable change in the behavior of the marginal quantities. We further note that the extension of the quantum state in position direction is larger than that in momentum direction consistent with the behaviors of the marginal distributions observed in Figs. 4(d) and 4(e).

### B. Husimi function of the CT model

To analyze the ESQPT in the CT model we propose the following quench protocol. We prepare initially the system in the ground state,  $|\Psi_0\rangle$ , of  $\hat{H}_{\text{CT}}$  with  $\xi = \xi_0 > 1$ . Then, we suddenly change the coupling strength from  $\xi_0$  to  $\xi_1$  and consider the evolution of the system, governed by Hamiltonian  $\hat{H}_{\text{CT}}(\xi_1)$ . As it has been already pointed out in the LMG model, the sudden quench process increases the system energy, resulting in a final rescaled energy  $\mathcal{E}_{\text{CT}}(\xi_0, \xi_1) = \langle \Psi_0 | \hat{H}_{\text{CT}} | \Psi_0 \rangle / j$ . The dependence of  $\mathcal{E}_{\text{CT}}(\xi_0, \xi_1)$  on  $\xi_1$ , for a fixed  $\xi_0$  value, implies that different ESQPT phases can be accessed by the variation of  $\xi_1$ . As seen in Fig. 7, depending on the  $\xi_0$  and  $\xi_1$  values, the final energy  $\mathcal{E}_{\text{CT}}(\xi_0, \xi_1)$  will be such to drive the system to one of the two possible ESQPT phases. For a given  $\xi_0$  value, the critical quench strength,

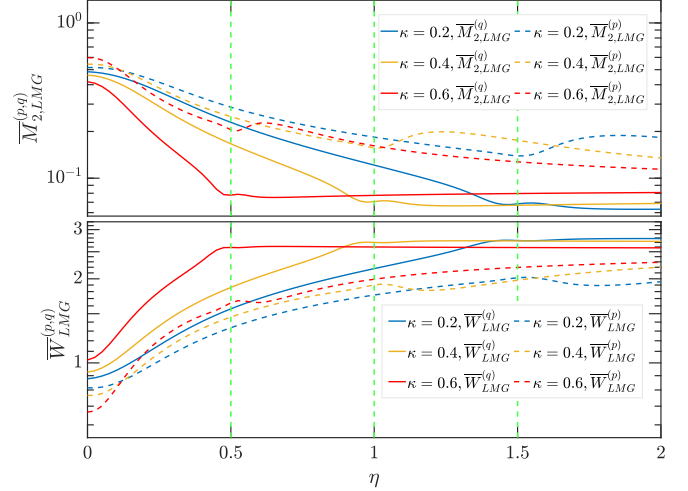


FIG. 6. Second moment (upper panel) and Wehrl entropy (bottom panel) of the marginal distributions of  $\overline{Q}_{\text{LMG}}(p, q)$  as a function of  $\eta$  for several  $\kappa$  values with  $j = N/2 = 200$ . The vertical green dashed lines in both panels mark the critical values  $\eta_c$  for each corresponding  $\kappa$ . The axes in all panels are dimensionless.

denoted as  $\xi_1^c$ , can be identified making the final energy equals to the critical ESQPT energy:  $\mathcal{E}_{\text{CT}}(\xi_0, \xi_1) = E_c/j = -2$ . By using the semiclassical approach (see Appendix B), one can find that  $\xi_1^c$  is given by

$$\xi_1^c = \frac{2\xi_0}{\xi_0 + 1}, \quad (20)$$

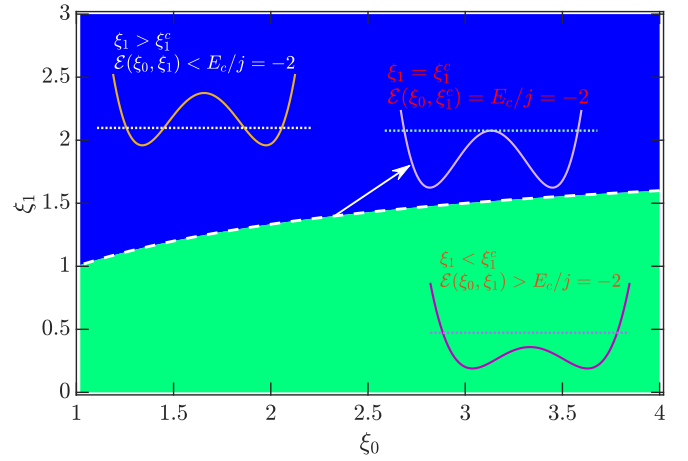


FIG. 7. Schematic illustration of the excited state phase diagram of the CT model. The ground state of  $\hat{H}_{\text{CT}}$  at  $\xi_0 > 1$  is quenched to  $\xi_1$ , which results in two different phases with critical line takes place at  $\xi_1^c = 2\xi_0/(\xi_0 + 1)$ . For  $\xi_1 > \xi_1^c$ , the quenched system has energy less than the critical energy of ESQPT,  $\mathcal{E}_{\text{CT}}(\xi_0, \xi_1) < E_c/j = -2$ , while the quenched energy is greater than  $E_c/j = -2$  when  $\xi_1 > \xi_1^c$ . At the critical quench  $\xi_1 = \xi_1^c$ , the quenched energy equals to the critical energy of ESQPT. In addition, two phases are also identified in the different classical dynamics of a classical particle in a double well potential, which exhibits the localized behaviors for  $\xi_1 > \xi_1^c$ , whereas it displays delocalized behaviors as long as  $\xi_1 > \xi_1^c$ . The white dashed line indicates the critical line  $\xi_1^c$ . Further details are discussed in the main text. The axes in the figure are dimensionless.

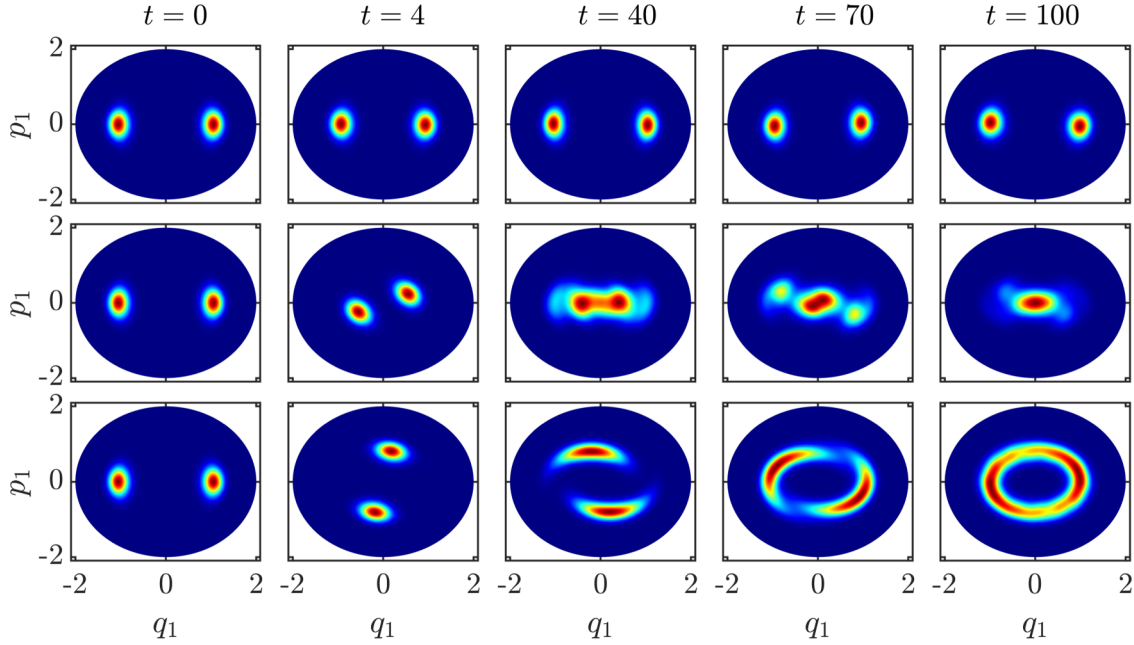


FIG. 8. Snapshots of the rescaled spin Husimi function  $\mathcal{Q}_t(p_1, q_1) = Q_t(p_1, q_1)/Q_t^m(p_1, q_1)$  with  $Q_t^m(p_1, q_1)$  being the maximum value of  $Q_t(p_1, q_1)$ , at different time steps for the CT model with  $\xi_1 = 2.5, 1.5, 0.5$  (from top to bottom). Other parameters are:  $j = 30$  and  $\xi_0 = 3$ . The color scale of Fig. 3 has been used. The axes in all figures are dimensionless.

with  $\xi_0 > 1$ . The critical coupling of the ESQPT depends on the value of  $\xi_0$  and is always larger than the critical value of the control parameter for the ground-state QPT,  $\xi_c = 1$ .

Once evolved, the state of the model is  $\rho_t(\xi_1) = |\Psi_t\rangle\langle\Psi_t| = e^{-i\hat{H}(\xi_1)t}\rho_0(\xi_0)e^{i\hat{H}(\xi_1)t}$  with  $\rho_0(\xi_0) = |\Psi_0\rangle\langle\Psi_0|$ . As the phase space of the coupled top model has four dimensions, the Husimi function, expressed in terms of  $\rho_t(\xi_1)$ , takes the form

$$\mathcal{Q}_t(\mathbf{p}, \mathbf{q}) = \langle\Upsilon(\mathbf{p}, \mathbf{q})|\rho_t(\xi_1)|\Upsilon(\mathbf{p}, \mathbf{q})\rangle, \quad (21)$$

where  $\mathbf{p} = (p_1, p_2)$ ,  $\mathbf{q} = (q_1, q_2)$ , and  $|\Upsilon(\mathbf{p}, \mathbf{q})\rangle = |\zeta(p_1, q_1)\rangle \otimes |\zeta(p_2, q_2)\rangle$  with

$$\zeta(p_k, q_k) = \frac{q_k - ip_k}{\sqrt{4 - (p_k^2 + q_k^2)}}, \quad k = 1, 2.$$

The normalization condition for  $\mathcal{Q}_t(\mathbf{p}, \mathbf{q})$  reads

$$\left(\frac{2j+1}{4\pi}\right)^2 \int_{\Omega_1} \int_{\Omega_2} \mathcal{Q}_t(\mathbf{p}, \mathbf{q}) d\mathbf{p} d\mathbf{q} = 1, \quad (22)$$

where  $\Omega_1 \in \{(p_1, q_1) | p_1^2 + q_1^2 \leq 4\}$  and  $\Omega_2 \in \{(p_2, q_2) | p_2^2 + q_2^2 \leq 4\}$ .

The four-dimensional Husimi function  $\mathcal{Q}_t(\mathbf{p}, \mathbf{q})$  is difficult to visualize. Therefore, we consider the projection of the Husimi function over the space  $(p_1, q_1)$ , so that  $\mathcal{Q}_t(p_1, q_1) \sim \int dp_2 dq_2 \mathcal{Q}_t(\mathbf{p}, \mathbf{q})$ . As the coherent states  $|\zeta(p_2, q_2)\rangle$  in the space  $(p_2, q_2)$  fulfill the normalization condition [cf. Eq. (3)], the projected Husimi function adopts the form

$$\mathcal{Q}_t(p_1, q_1) = \langle\zeta(p_1, q_1)|\rho_t^1(\xi_1)|\zeta(p_1, q_1)\rangle, \quad (23)$$

with a normalization condition

$$\frac{2j+1}{4\pi} \int_{\Omega_1} \mathcal{Q}_t(p_1, q_1) dp_1 dq_1 = 1.$$

Here  $\rho_t^1(\xi_1) = \text{Tr}_2[\rho_t(\xi_1)]$  is the reduced density matrix of the first spin.

In Fig. 8, we plot snapshots of the evolution of the CT model Husimi function at several time steps for  $\xi_0 = 3$  and  $\xi_1 = 0.5, 1.5, 2.5$ . The critical  $\xi_1$  value in this case is  $\xi_1^c = 1.5$  [cf. Eq. (20)]. The ground state of the coupled top model has even-parity and even coherent states provide a good approximation. The Husimi function at the initial time consists of two distinct wave packets, symmetrically placed in the phase space, as seen in the first column of Fig. 8. As time increases, the Husimi function of the CT model follows an evolution very similar the one observed in the LMG model case [cf. Fig. 3]. Namely, two different wave packets can be distinguished in the evolution of the Husimi function until  $\xi_1 = \xi_1^c$ , when the two separated wave packets finished merging. If the value of  $\xi_1$  is further decreased, then the two disconnected wave packets finish merging into a single packet at large time values. Therefore, as in the LMG model, the ESQPT in the CT model can also be identified through the particular dynamics of the Husimi function.

As in the LMG model case, the essentials of the dynamical behavior of the CT model shown in Fig. 8 can be captured by a simple classical model involving only one degree of freedom. In the classical limit, the CT model dynamics for a single degree of freedom is described by a classical particle, with coordinate  $q_1$ , confined by a one-dimensional double well potential,  $\mathcal{V}_{\text{CT}}^c(q_1)$  (see Appendix C for more details). Then, as we have already discussed in the LMG model and as shown in the insets of Fig. 7, for  $\xi_1 > \xi_1^c$  the resulting energy is  $\mathcal{E}_{\text{CT}}(\xi_0, \xi_1) < E_c/j$  and the particle does not have enough energy to surpass the central barrier. Thus it remains trapped in one of the two wells, depending on its initial configuration and the phase space in this case consists of two disconnected and symmetrical components. Conversely, for  $\xi_1 < \xi_c$  the energy



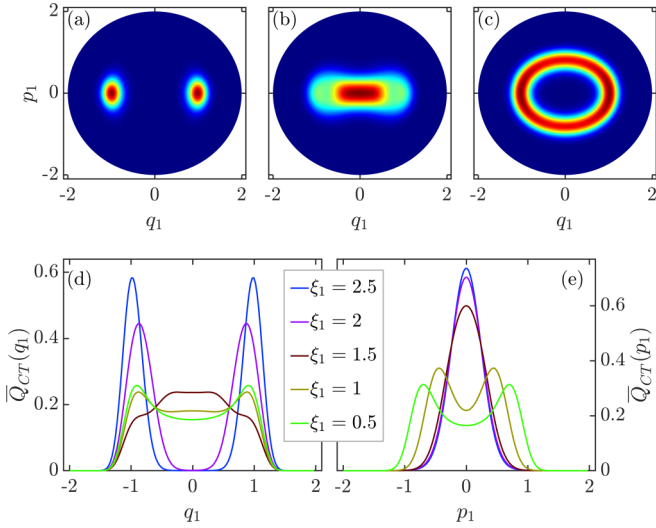


FIG. 9. Rescaled long-time averaged Husimi function  $\overline{Q}_{CT}(p_1, q_1) = \overline{Q}_{CT}(p_1, q_1) / \overline{Q}_{CT,m}$  of the CT model for (a)  $\xi_1 = 2.5$ , (b)  $\xi_1 = 1.5$ , and (c)  $\xi_1 = 0.5$ . By  $\overline{Q}_{CT,m}$  we denote the maximum value of  $\overline{Q}_{CT}(p_1, q_1)$ . The color scale in Fig. 3 has been employed for panels (a–c). Marginal distributions  $\overline{Q}_{CT}(q_1)$  (d) and  $\overline{Q}_{CT}(p_1)$  (e) of  $\overline{Q}_{CT}(p_1, q_1)$  for several values of  $\xi_1$  (see legend). All panels:  $j = 30$  and  $\xi_0 = 3$ . The axes in all panels are dimensionless.

is larger than the critical energy value,  $\mathcal{E}_{CT}(\xi_0, \xi_1) > E_c/j$ , and the classical particle has enough energy go from one well to the other through the origin. This leads to the merging of the previously disconnected two phase space regions into a single one. At  $\xi_1 = \xi_1^c$ , the system energy is  $\mathcal{E}_{CT}(\xi_0, \xi_1) = E_c/j$ , and the particle starts straddling both wells for the first time. At this energy, the motion of particle starts the fusing of the two distinct phase space regions. More details of the classical dynamics for one degree of freedom of the CT model are given in Appendix C.

We can now check if more conspicuous CT model ESQPT signatures are revealed in the features of long-time averaged Husimi function Eq. (17). In this case, the long-time averaged function can be written as

$$\overline{Q}_{CT}(p_1, q_1) = \langle \zeta(p_1, q_1) | \overline{\rho}_1(\xi_1) | \zeta(p_1, q_1) \rangle, \quad (24)$$

where  $\overline{\rho}_1(\xi_1) = \text{Tr}_2[\overline{\rho}(\xi_1)]$  with

$$\overline{\rho}(\xi_1) = \lim_{T \rightarrow \infty} \frac{1}{T} \int_0^T \rho_t(\xi_1) dt.$$

In the eigenstates of the post-quench Hamiltonian  $\hat{H}_{CT}(\xi_1)$ , denoted by  $\{|E_n\rangle\}$ , it is then straightforward that  $\overline{Q}_{CT}(p_1, q_1)$  can be calculated as

$$\overline{Q}_{CT}(p_1, q_1) = \sum_n |\langle \Psi_0 | E_n \rangle|^2 \langle \zeta(p_1, q_1) | \rho_1^{(n)}(\xi_1) | \zeta(p_1, q_1) \rangle, \quad (25)$$

where  $\rho_1^{(n)}(\xi_1) = \text{Tr}_2(|E_n\rangle\langle E_n|)$ . As we found in the LMG model,  $\overline{Q}_{CT}(p_1, q_1)$  for the coupled top model depends on the transition probability between the initial state and the eigenstates of  $\hat{H}_{CT}(\xi_1)$ .

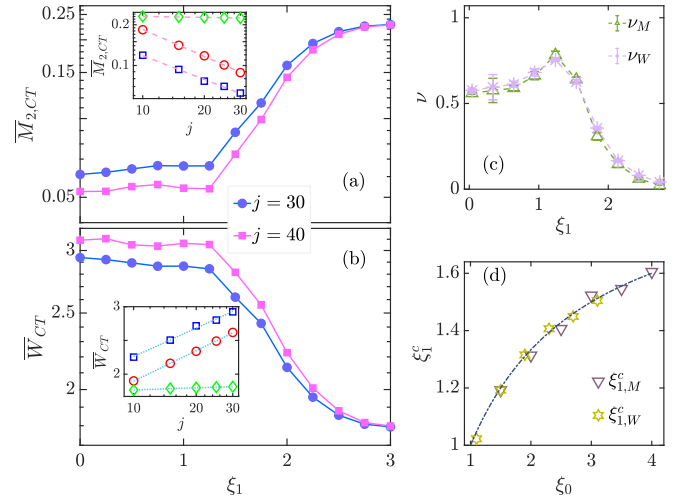


FIG. 10. (a) Second moment of  $\overline{Q}_{CT}(p_1, q_1)$  as a function of  $\xi_1$  for different system sizes,  $j$ , with  $\xi_0 = 3$  and  $\xi_1^c = 1.5$  [see Eq. (20)]. Inset:  $\overline{M}_{2,CT}$  as a function of  $j$  at  $\xi_1 = 0.3$  (blue squares),  $\xi_1 = 1.5$  (red circles), and  $\xi_1 = 2.7$  (green diamonds). Dashed lines are functions of the form  $\overline{M}_{2,CT} \sim j^{-\nu_M}$ . (b) Wehrl entropy of  $\overline{Q}_{CT}(p_1, q_1)$  as a function of  $\xi_1$  for different  $j$  with  $\xi_0 = 3$ . Inset:  $\overline{W}_{CT}$  as a function of  $j$  for  $\xi_1 = 0.3$  (blue squares),  $\xi_1 = 1.5$  (red circles), and  $\xi_1 = 2.7$  (green diamonds). Dotted lines have a dependence  $\overline{W}_{CT} \sim \nu_W \ln(j)$ . (c) Finite-size scaling exponents  $\nu_M$  and  $\nu_W$  as a function of  $\xi_1$  with  $\xi_0 = 3$ . (d) Estimated critical points  $\xi_{1,M}^c$ ,  $\xi_{1,W}^c$ , obtained from the minima in  $d\nu_{M(W)}/d\xi_1$ , as a function of  $\xi_0$ . The dot-dashed line denotes the analytical result from Eq. (20). All quantities are unitless.

In Figs. 9(a)–9(c), we plot  $\overline{Q}_{CT}(p_1, q_1)$  for  $\xi_0 = 3$ ,  $\xi_1 = 0.5, 1.5, 2.5$  and a system size  $j = 30$ . For decreasing  $\xi_1$  values, the Husimi function undergoes a noticeable change when  $\xi_1$  goes through its critical value  $\xi_1^c = 1.5$ . The ESQPT at  $\xi_1^c = 1.5$  is clearly associated with a significant extension of the phase space surface covered by the Husimi function. The changes of  $\overline{Q}_{CT}(p_1, q_1)$  in phase space for decreasing  $\xi_1$  value can be better appreciated in the marginal distributions, depicted in Figs. 9(d) and 9(e). Consequently, the occurrence of the ESQPT in the CT model is marked by a significant increase of the extension of the Husimi function in phase space, as observed in the LMG model.

To provide further insight into the ESQPT phase space signatures in the CT model, we consider the second moment and the Wehrl entropy of  $\overline{Q}_{CT}(p_1, q_1)$ . In Figs. 10(a) and 10(b), we plot  $\overline{M}_{2,CT}$  and  $\overline{W}_{CT}$ , respectively, as a function of  $\xi_1$  with  $\xi_0 = 3$  for two different system sizes,  $j = 30, 40$ . The critical value of  $\xi_1$  for  $\xi_0 = 3$  is  $\xi_1^c = 1.5$ . The significant change in  $\overline{M}_{2,CT}$  and  $\overline{W}_{CT}$  as  $\xi_1$  passes through the critical value is clearly visible. For  $\xi_1 < \xi_1^c = 1.5$ , the Husimi function has maximum extension and  $\overline{M}_{2,CT}$  ( $\overline{W}_{CT}$ ) is roughly constant at a minimum (maximum) value and decreases (increases) for increasing  $j$  values. However, in the  $\xi_1 > \xi_1^c$  case, we observe that  $\overline{M}_{2,CT}$  ( $\overline{W}_{CT}$ ) increases (decreases) as  $\xi_1$  increases. These results suggest that the largest extension of the Husimi function in phase space can be considered a key ESQPT signature. We further find that  $\overline{M}_{2,CT}$  follows a power-law scaling with the system size of the form  $\overline{M}_{2,CT} \sim j^{-\nu_M}$  with a scaling exponent  $\nu_M$  that depends on the value of  $\xi_1$ , as shown in the inset of Fig. 10(a). However, the Wehrl entropy exhibits a logarithmic

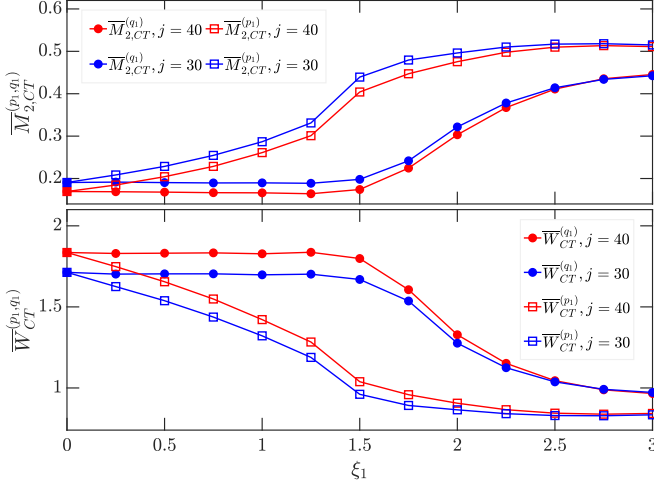


FIG. 11. Second moment (upper panel) and Wehrl entropy (bottom panel) of the marginal distributions of  $\bar{Q}_{CT}(p_1, q_1)$  as a function of  $\xi_1$  for different  $j$  with  $\xi_0 = 3$  and  $\xi_1^c = 1.5$ . All quantities are unitless.

mic scaling with the system size,  $\bar{W}_{CT} \sim \nu_W \ln(j)$ , where  $\nu_W$  varies with  $\xi_1$  [see inset in Fig. 10(b)]. The dependence of  $\nu_M$  and  $\nu_W$  with  $\xi_1$  is shown in Fig. 10(c), where it is clear how both quantities behave differently in the two phases. In particular, they both reach a maximum, followed by a rapid decrease, at the critical point; suggesting that it is possible to identify the ESQPT critical point as the location of the minima points in the derivatives of  $\nu_M$  and  $\nu_W$  with respect to  $\xi_1$ . Our numerically estimated critical points, together with the analytical ones obtained from Eq. (20), are plotted in Fig. 10(d), with a fine agreement between the results obtained with both approaches.

In Fig. 11, we depict the second moment and the Wehrl entropy of the marginal distributions of the Husimi function as a function of  $\xi_1$  for  $\xi_0 = 3$  and system size  $j = 30, 40$ . As expected, the marginal quantities undergo a sudden change as the system goes through the  $\xi_1$  value that corresponds with the ESQPT critical point. Moreover, as observed in the LMG model, the Husimi function of the CT model also exhibits a more significant extension in the position marginal than in the momentum marginal.

## V. CONCLUSIONS

We have studied the phase space signatures of the ESQPT in two different models, the Lipkin-Meshkov-Glick and coupled top models, by means of the Husimi quasiprobability distribution. Both models exhibit an ESQPT associated with a second-order ground-state QPT, but due to their different effective degrees of freedom, the ESQPT in the LMG model results in a cusp-like nonanalyticity in the density of states, while in the CT model the ESQPT presence is revealed in the first derivative of the density of states. We have showed that phase space signatures of the ESQPT in these two models can be identified through different properties of their Husimi functions and the marginal distributions. We have found that the different ESQPT phases can be identified by a distinct dynamical behavior of the Husimi function. In fact, the dynamics

of the Husimi function allows for the detection of the ESQPT presence in both models. We have also demonstrated that the long-time average of the Husimi function exhibits distinct features in different phases of ESQPT. The transition of the long-time averaged Husimi function from two symmetrically localized wave packets to a single extended wave packet is the main signature of the occurrence of an ESQPT in phase space. To quantify the phase space spreading of the long time averaged Husimi function, we further investigated the properties of the second moment and the Wehrl entropy of the long-time averaged Husimi function and its marginal distributions. The singular features observed in these two quantities, the second moment and the Wehrl entropy, represent a visible manifestation of ESQPT. In turn, we have employed these two singular features to estimate the location of the critical energy of the ESQPT, obtaining a very satisfactory agreement between numerical estimations and analytical results.

Our findings confirm that phase space methods are a powerful tool in the understanding of ESQPTs in many-body quantum systems, extending the results published in the literature, that focus mainly in the phase space signatures of ground-state quantum phase transitions. As the kind of ESQPTs studied in this work are quite general [75], other systems like the Rabi [44] and Dicke models [40,41] are expected to exhibit similar signatures in phase space. It is an interesting future prospect to systematically explore the phase space signatures of ESQPTs in various many-body systems. Another appealing extension of the present work would be to explore the phase space signatures of ESQPTs associated with a first-order ground-state QPT [43]. Finally, given that the Husimi function has been measured in several experiments [116–119], and that it is possible to obtain realizations of the two models studied in this work in quantum simulators [52,100,109,120], we expect that the present results can be experimentally tested.

## ACKNOWLEDGMENTS

Q.W. acknowledges support from the National Science Foundation of China under Grant No. 11805165, Zhejiang Provincial Nature Science Foundation under Grant No. LY20A050001, and Slovenian Research Agency (ARRS) under the Grants No. J1-9112 and No. P1-0306. This work has also been partially supported by the Consejería de Conocimiento, Investigación y Universidad, Junta de Andalucía and European Regional Development Fund (ERDF), Ref. No. SOMM17/6105/UGR and by the Ministerio de Ciencia, Innovación y Universidades (Ref. No. COOPB20364). F.P.-B. also thanks support from Project No. UHU-1262561. Computing resources supporting this work were partly provided by the CEAFCM and Universidad de Huelva High Performance Computer (HPC@UHU) located in the Campus Universitario el Carmen and funded by FEDER/MINECO Project No. UNHU-15CE-2848.

## APPENDIX A: CLASSICAL LIMIT OF THE LMG AND CT MODELS

The classical limit of the LMG and CT models can be achieved in the limit  $j \rightarrow \infty$ , and the corresponding classical

equations of motions (EOMs) are obtained from the semiclassical approach. To see this, we first employ the relations

$$\langle \zeta | J_+ | \zeta \rangle = \frac{2j\zeta^*}{1+|\zeta|^2}, \quad \langle \zeta | J_- | \zeta \rangle = \frac{2j\zeta}{1+|\zeta|^2}, \quad \langle \zeta | J_z | \zeta \rangle = j \left( \frac{|\zeta|^2 - 1}{|\zeta|^2 + 1} \right), \quad (\text{A1})$$

where  $J_{\pm} = J_x \pm iJ_y$ . Then, it is straightforward to find the rescaled expectation value of the LMG and CT Hamiltonians in the coherent state are, respectively, given as

$$H_{\text{LMG}}(\zeta) = \frac{\langle \zeta | \hat{H}_{\text{LMG}} | \zeta \rangle}{j} = -2(1-\kappa) \left( \frac{\zeta + \zeta^*}{|\zeta|^2 + 1} \right) + \kappa j \left( \frac{|\zeta|^2 - 1}{|\zeta|^2 + 1} + 1 \right), \quad (\text{A2})$$

$$H_{\text{CT}}(\zeta_1, \zeta_2) = \frac{\langle \zeta_1, \zeta_2 | \hat{H}_{\text{CT}} | \zeta_1, \zeta_2 \rangle}{j} = j \left[ \frac{|\zeta_1|^2 - 1}{|\zeta_1|^2 + 1} + \frac{|\zeta_2|^2 - 1}{|\zeta_2|^2 + 1} + \xi \frac{(\zeta_1^* + \zeta_1)(\zeta_2^* + \zeta_2)}{(1+|\zeta_1|^2)(1+|\zeta_2|^2)} \right]. \quad (\text{A3})$$

By replacing the Bloch parameter  $\zeta$  with the classical canonical variables  $(p, q)$  [cf. Eq. (4) in main text], the explicit form of the corresponding classical Hamiltonians read

$$\mathcal{H}_{\text{LMG}}^c = \frac{\kappa}{2}(p^2 + q^2) + \frac{1-\kappa}{2}q^2(p^2 + q^2) - 2(1-\kappa)q^2, \quad \mathcal{H}_{\text{CT}}^c = \frac{1}{2}(p_1^2 + q_1^2) + \frac{1}{2}(p_2^2 + q_2^2) - 2 + \frac{\xi}{4}q_1q_2\mathcal{G}_1\mathcal{G}_2, \quad (\text{A4})$$

where  $\mathcal{G}_1 = \sqrt{4 - (p_1^2 + q_1^2)}$  and  $\mathcal{G}_2 = \sqrt{4 - (p_2^2 + q_2^2)}$ . Finally, the classical EOMs of the LMG model take the form

$$\dot{q} = \frac{\partial \mathcal{H}_{\text{LMG}}^c}{\partial p} = \kappa p + (1-\kappa)pq^2, \quad \dot{p} = -\frac{\partial \mathcal{H}_{\text{LMG}}^c}{\partial q} = (4-5\kappa)q - (1-\kappa)p^2q - 2(1-\kappa)q^3, \quad (\text{A5})$$

while the classical EOMs of the CT model are

$$\begin{aligned} \dot{q}_1 &= \frac{\partial \mathcal{H}_{\text{CT}}^c}{\partial p_1} = p_1 - \frac{\xi \mathcal{G}_2}{4\mathcal{G}_1} q_1 q_2 p_1, & \dot{p}_1 &= -\frac{\partial \mathcal{H}_{\text{CT}}^c}{\partial q_1} = -q_1 + \frac{\xi \mathcal{G}_2}{4\mathcal{G}_1} q_2 q_1^2 - \frac{\xi}{4} \mathcal{G}_1 \mathcal{G}_2 q_2, \\ \dot{q}_2 &= \frac{\partial \mathcal{H}_{\text{CT}}^c}{\partial p_2} = p_2 - \frac{\xi \mathcal{G}_1}{4\mathcal{G}_2} q_1 q_2 p_2, & \dot{p}_2 &= -\frac{\partial \mathcal{H}_{\text{CT}}^c}{\partial q_2} = -q_2 + \frac{\xi \mathcal{G}_1}{4\mathcal{G}_2} q_1 q_2^2 - \frac{\xi}{4} \mathcal{G}_1 \mathcal{G}_2 q_1. \end{aligned} \quad (\text{A6})$$

## APPENDIX B: ESQPT CRITICAL QUENCH PARAMETERS IN THE LMG AND CT MODELS

In the classical limit, the ground state of a quantum system can be represented by the fixed points that minimize the classical Hamiltonian. By setting  $\nabla \mathcal{H}^c = 0$  for the LMG and CT models, the fixed points of these models are given by

$$(p_f, q_f)_{\text{LMG}} = \begin{cases} (0, 0) & \text{for } \kappa \geq \kappa_c, \\ (0, \pm \sqrt{\frac{4-5\kappa}{2(1-\kappa)}}) & \text{for } 0 < \kappa < \kappa_c, \end{cases} \quad (\text{B1})$$

$$\begin{aligned} (\mathbf{p}_f, \mathbf{q}_f)_{\text{CT}} &= (p_1^f, p_2^f, q_1^f, q_2^f)_{\text{CT}} \\ &= \begin{cases} (0, 0, 0, 0) & \text{for } \xi \leq 1, \\ (0, 0, \pm \sqrt{\frac{2(\xi-1)}{\xi}}, \mp \sqrt{\frac{2(\xi-1)}{\xi}}) & \text{for } \xi > 1. \end{cases} \end{aligned} \quad (\text{B2})$$

The ground states of both models can be written as

$$\begin{aligned} |\Psi_0\rangle_{\text{LMG}} &= |\zeta(p_f, q_f)\rangle, \\ |\Psi_0\rangle_{\text{CT}} &= |\zeta(p_1^f, q_1^f)\rangle \otimes |\zeta(p_2^f, q_2^f)\rangle. \end{aligned} \quad (\text{B3})$$

As pointed out in the main text, we initialize the LMG and CT models in the ground state with  $0 < \kappa < \kappa_c$  and  $\xi > 1$ , respectively.

In our study, the sudden change of the control parameter leads to the variation of the energy of system. As the system is initially in the ground state of the initial Hamiltonian, larger quenches transfer a larger amount of energy onto the system. The rescaled energy of the final quenched state for the LMG

and CT models are given by

$$\mathcal{E}_{\text{LMG}}(\kappa, \eta) = \text{LMG} \langle \Psi_0 | \hat{H}_{\text{LMG}}^f | \Psi_0 \rangle_{\text{LMG}} / j, \quad (\text{B4})$$

$$\mathcal{E}_{\text{CT}}(\xi_0, \xi_1) = \text{CT} \langle \Psi_0 | \hat{H}_{\text{CT}}^f | \Psi_0 \rangle_{\text{CT}} / j, \quad (\text{B5})$$

where  $\hat{H}_{\text{LMG}}^f = \hat{H}_{\text{LMG}} + \eta(\hat{J}_z + N/2)$  and  $\hat{H}_{\text{CT}} = \hat{H}_{\text{CT}}(\xi_1)$ . By inserting Eqs. (B1)–(B3) into the equations given above, and using Eq. (A1), after some algebra, one can find that the energy of the quenched state can be expressed as follows:

$$\mathcal{E}_{\text{LMG}}(\kappa, \eta) = \frac{\eta(4-5\kappa)}{4(1-\kappa)} - \frac{(4-5\kappa)^2}{8(1-\kappa)}, \quad (\text{B6})$$

$$\mathcal{E}_{\text{CT}}(\xi_0, \xi_1) = \frac{(\xi_0 - 1)[2\xi_0 - \xi_1(\xi_0 + 1)]}{\xi_0^2} - 2. \quad (\text{B7})$$

As an ESQPT is identified by the critical energy  $E_c$ , the critical quench parameter is, therefore, obtained when the energy of the quenched state reaches  $E_c$ . By setting Eqs. (B6) and (B7) equal to the critical energy of the LMG model and CT model, respectively, we finally find the values of the critical parameters  $\eta_c$  and  $\xi_1^c$ ,

$$\eta_c = 2 - \frac{5}{2}\kappa, \quad \xi_1^c = \frac{2\xi_0}{\xi_0 + 1}, \quad (\text{B8})$$

with  $0 < \kappa < \kappa_c$  and  $\xi_0 > 1$ . These expressions have already been given in the main text [cf. Eqs. (15) and (20)].

Therefore, the ESQPT in LMG and CT models sits at the saddle point of their classical double well potential [59]. This leads to fundamental differences in the particle dynamics in the different ESQPT phases, as we have already discussed in the main text. This will be further demonstrated by means

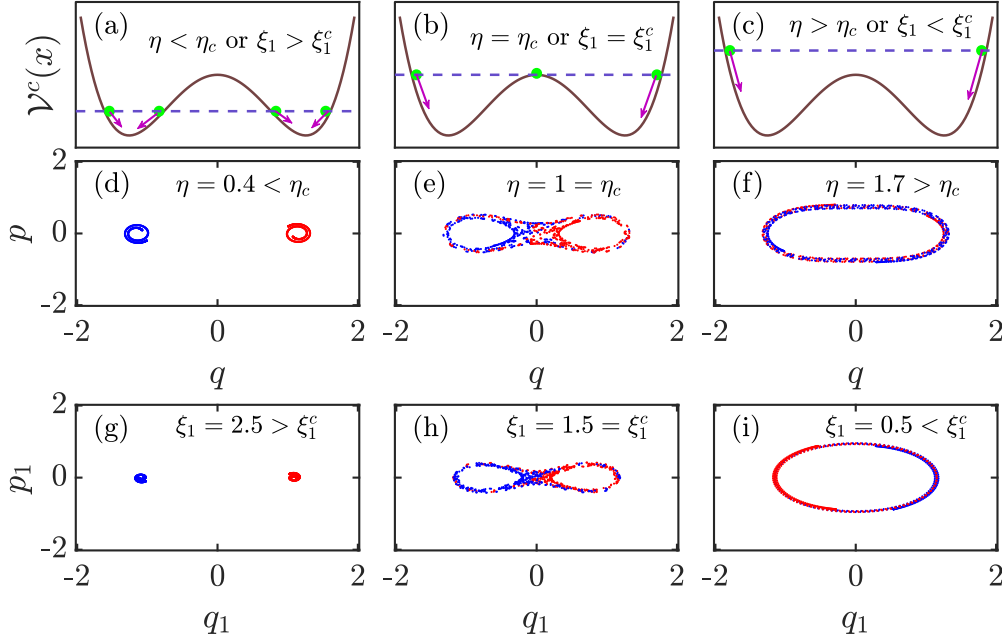


FIG. 12. In the classical limit, both LMG and CT models can be described as a particle (green dot) in a double well potential  $\mathcal{V}^c(x)$  with  $x = q$  (for the LMG model) and  $x = q_1$  (for the CT model). The particle's energy is indicated by a violet dashed line. If the quantum quench leads to a particle with an energy lower than the top of the potential barrier [panel (a)], then the particle stays confined into either the left or right well. In the critical quench case [panel (b)], the energy of the particle equals the height of the central barrier, and the particle is able to explore the origin for the first time. In case that after the quench the particle's energy is larger than the central barrier [panel (c)], the particle can surpass the central barrier and it moves periodically between the two wells. Panels (d)–(f): Snapshots of the classical dynamics of the LMG model for different  $\eta$ , a maximum time  $t = 200$ , and  $\kappa = 0.4$ . Blue dots correspond to an initial condition with  $q < 0$ , while red dots correspond to an initial condition with  $q > 0$ . Panels (g)–(i): Snapshots of the classical dynamics of the CT model for different  $\xi_1$ , a maximum time  $t = 700$ , and  $\xi_0 = 3$ . As in the LMG model, blue and red dots in each panel correspond to different initial conditions,  $q_1 < 0$  (blue) and  $q_1 > 0$  (red). All quantities are unitless.

of the classical dynamics. In particular, we show in the next Appendix that the separatrix in the phase space marks the ESQPT.

### APPENDIX C: CLASSICAL DYNAMICS OF THE LMG AND CT MODELS

The dynamical features in the different phases of an ESQPT can be captured by an effective model that describes a classical particle confined within a double well potential.

For the LMG model, by setting  $p = 0$  in its classical Hamiltonian, one can find the potential can be written as

$$\mathcal{V}_{\text{LMG}}^c(q) = \frac{1 - \kappa}{2} q^4 - \frac{4 - 5\kappa}{2} q^2. \quad (\text{C1})$$

The potential  $\mathcal{V}_{\text{LMG}}^c(q)$  has a symmetric double-well shape when  $0 < \kappa < \kappa_c$ , with minima at  $q = \pm\sqrt{(4 - 5\kappa)/(2 - 2\kappa)}$  and a local maximum at  $q = 0$ . The double-well potential for the CT model is also derived from its classical Hamiltonian by letting  $p_1 = p_2 = 0$ . Moreover, as the fixed points for  $\xi > 1$  satisfy  $q_2 = -q_1$  [cf. Eq. (B2)], we further set  $q_2 = -q_1$ , which allows us to express the potential exclusively as a function of  $q_1$  as

$$\mathcal{V}_{\text{CT}}^c(q_1) = \frac{\xi}{4} q_1^4 - (\xi - 1) q_1^2 - 2. \quad (\text{C2})$$

For  $\xi > 1$ , the shape of  $\mathcal{V}_{\text{CT}}^c(q_1)$  again has a symmetric double-well shape, with minima at  $q_1 = \pm\sqrt{2(\xi - 1)/\xi}$  and a local maximum at  $q_1 = 0$ . Hence, the potential  $\mathcal{V}_{\text{CT}}^c(q_1)$  structure is completely equivalent to the structure of potential  $\mathcal{V}_{\text{LMG}}^c(q)$ . The ESQPT critical energy in the LMG and CT models is defined as the difference between the potential value at the central maximum and its minimum value [59].

As initially the system is in the ground state, one can assume that the classical particle is located at one of the fixed points, either the left one or the right one. The quantum quench provoked by the variation of the control parameter is akin to a sudden increase in the energy of the classical particle. Therefore, the final energy of the quenched particle and the relative height of the potential barrier determine the dynamics of the classical particle. Whenever the quenched particle has an energy lower than the critical energy, the particle cannot straddle the central barrier and remains confined either in the left or the right well, as shown in Fig. 12(a). In the critical quench case, as the energy of the particle matches the critical energy, the particle overcomes the central barrier for the first time [Fig. 12(b)]. Finally, once the energy of the quenched particle lies above the barrier, the particle surpasses the barrier and moves periodically between both wells, as seen in Fig. 12(c).

The resulting classical dynamics for the LMG and CT models for distinct quenches are plotted in the second and third rows of Fig. 12, respectively. They are obtained by

solving the classical EOMs in Eqs. (A5) and (A6) with initial conditions given by Appendix B. In both models, the confined motion of the particle for the case with a quenched particle energy below the critical value can be clearly identified by the existence of two disconnected phase space regions. These two regions start to merge once the quenched particle energy reaches the critical value, which allows the particle to overcome the central barrier. Moreover, for both models,

the phase space separatrix is clearly visible at the critical energy of ESQPT. As soon as the quenched particle energy is larger than the critical value, the particle visits both wells, and the two disconnected regions merge into a single one. Finally, it is worth to emphasize the remarkable agreement that exists between the classical dynamics and the time evolution of the Husimi functions discussed in the main text.

- 
- [1] H. Weyl, *Z. Phys.* **46**, 1 (1927).
- [2] E. Wigner, *Phys. Rev.* **40**, 749 (1932).
- [3] H. Weyl, *The Theory of Groups and Quantum Mechanics* (Courier Corporation, Chelmsford, MA, 1950).
- [4] C. K. Zachos, D. B. Fairlie, and T. L. Curtright, *Quantum Mechanics in Phase Space: An Overview with Selected Papers* (World Scientific, Singapore, 2005).
- [5] F. E. Schroeck Jr., *Quantum Mechanics on Phase Space* (Springer Science & Business Media, Berlin, 2013), Vol. 74.
- [6] M. Hillery, R. O'Connell, M. Scully, and E. Wigner, *Phys. Rep.* **106**, 121 (1984).
- [7] H.-W. Lee, *Phys. Rep.* **259**, 147 (1995).
- [8] A. Polkovnikov, *Ann. Phys.* **325**, 1790 (2010).
- [9] K. Husimi, *Proc. Phys. Math. Soc. Jpn.* **22**, 264 (1940).
- [10] R. J. Glauber, *Phys. Rev.* **131**, 2766 (1963).
- [11] J. Weinbub and D. K. Ferry, *Appl. Phys. Rev.* **5**, 041104 (2018).
- [12] U. Seyfarth, A. B. Klimov, H. d. Guise, G. Leuchs, and L. L. Sanchez-Soto, *Quantum* **4**, 317 (2020).
- [13] B. Koczor, R. Zeier, and S. J. Glaser, *Phys. Rev. A* **101**, 022318 (2020).
- [14] J. E. Moyal, *Proc. Cambridge Phil. Soc.* **45**, 99 (1949).
- [15] T. Takabayasi, *Prog. Theor. Phys.* **11**, 341 (1954).
- [16] G. Torres-Vega and J. H. Frederick, *J. Chem. Phys.* **93**, 8862 (1990).
- [17] O. Bohigas, S. Tomsovic, and D. Ullmo, *Phys. Rep.* **223**, 43 (1993).
- [18] W. P. Schleich, *Quantum Optics in Phase Space* (John Wiley & Sons, New York, 2011).
- [19] K. W. Mahmud, H. Perry, and W. P. Reinhardt, *Phys. Rev. A* **71**, 023615 (2005).
- [20] P. B. Blakie, A. S. Bradley, M. J. Davis, R. J. Ballagh, and C. W. Gardiner, *Adv. Phys.* **57**, 363 (2008).
- [21] S. Nonnenmacher and A. Voros, *J. Stats. Phys.* **92**, 431 (1998).
- [22] F. Toscano, A. Kenfack, A. R. Carvalho, J. M. Rost, and A. M. Ozorio de Almeida, *Proc. R. Soc. A* **464**, 1503 (2008).
- [23] C. Aulbach, A. Wobst, G.-L. Ingold, P. Hänggi, and I. Varga, *New J. Phys.* **6**, 70 (2004).
- [24] C. M. Carmesin, P. Kling, E. Giese, R. Sauerbrey, and W. P. Schleich, *Phys. Rev. Research* **2**, 023027 (2020).
- [25] A. Altland and F. Haake, *Phys. Rev. Lett.* **108**, 073601 (2012).
- [26] A. Altland and F. Haake, *New J. Phys.* **14**, 073011 (2012).
- [27] O. Brodier, K. Mallick, and A. M. O. de Almeida, *J. Phys. A* **53**, 325001 (2020).
- [28] E. Romera, R. del Real, and M. Calixto, *Phys. Rev. A* **85**, 053831 (2012).
- [29] M. Calixto, R. del Real, and E. Romera, *Phys. Rev. A* **86**, 032508 (2012).
- [30] E. Romera, M. Calixto, and O. Castaños, *Phys. Scr.* **89**, 095103 (2014).
- [31] O. Castaños, M. Calixto, F. Pérez-Bernal, and E. Romera, *Phys. Rev. E* **92**, 052106 (2015).
- [32] M. Calixto and E. Romera, *Europhys. Lett.* **109**, 40003 (2015).
- [33] O. Castaños, S. Cordero, R. López-Peña, and E. Nahmad-Achar, *Phys. Scr.* **93**, 085102 (2018).
- [34] Z. Mzaouali, S. Campbell, and M. El Baz, *Phys. Lett. A* **383**, 125932 (2019).
- [35] R. López-Peña, S. Cordero, E. Nahmad-Achar, and O. Castaños, *Phys. Scr.* **96**, 035103 (2021).
- [36] L. Carr, *Understanding Quantum Phase Transitions* (CRC Press, Boca Raton, FL, 2010).
- [37] P. Cejnar, M. Macek, S. Heinze, J. Jolie, and J. Dobeš, *J. Phys. A: Math. Gen.* **39**, L515 (2006).
- [38] M. Caprio, P. Cejnar, and F. Iachello, *Ann. Phys.* **323**, 1106 (2008).
- [39] P. Stránský, M. Macek, and P. Cejnar, *Ann. Phys.* **345**, 73 (2014).
- [40] T. Brandes, *Phys. Rev. E* **88**, 032133 (2013).
- [41] M. A. Bastarrachea-Magnani, S. Lerma-Hernández, and J. G. Hirsch, *Phys. Rev. A* **89**, 032101 (2014).
- [42] V. M. Bastidas, P. Pérez-Fernández, M. Vogl, and T. Brandes, *Phys. Rev. Lett.* **112**, 140408 (2014).
- [43] P. Stránský and P. Cejnar, *Phys. Lett. A* **380**, 2637 (2016).
- [44] R. Puebla, M.-J. Hwang, and M. B. Plenio, *Phys. Rev. A* **94**, 023835 (2016).
- [45] J. P. J. Rodriguez, S. A. Chilingaryan, and B. M. Rodríguez-Lara, *Phys. Rev. A* **98**, 043805 (2018).
- [46] G.-L. Zhu, X.-Y. Lü, S.-W. Bin, C. You, and Y. Wu, *Front. Phys.* **14**, 52602 (2019).
- [47] J. Khalouf-Rivera, M. Carvajal, L. F. Santos, and F. Pérez-Bernal, *J. Phys. Chem. A* **123**, 9544 (2019).
- [48] P. Feldmann, C. Klempt, A. Smerzi, L. Santos, and M. Gessner, *Phys. Rev. Lett.* **126**, 230602 (2021).
- [49] D. Larese and F. Iachello, *J. Mol. Struct.* **1006**, 611 (2011).
- [50] D. Larese, F. Pérez-Bernal, and F. Iachello, *J. Mol. Struct.* **1051**, 310 (2013).
- [51] B. Dietz, F. Iachello, M. Miski-Oglu, N. Pietralla, A. Richter, L. von Smekal, and J. Wambach, *Phys. Rev. B* **88**, 104101 (2013).
- [52] T. Tian, H.-X. Yang, L.-Y. Qiu, H.-Y. Liang, Y.-B. Yang, Y. Xu, and L.-M. Duan, *Phys. Rev. Lett.* **124**, 043001 (2020).
- [53] J. Khalouf-Rivera, F. Pérez-Bernal, and M. Carvajal, *J. Quant. Spectrosc. Radiat. Transfer* **261**, 107436 (2021).
- [54] A. Relaño, J. M. Arias, J. Dukelsky, J. E. García-Ramos, and P. Pérez-Fernández, *Phys. Rev. A* **78**, 060102(R) (2008).

- [55] P. Pérez-Fernández, A. Relaño, J. M. Arias, J. Dukelsky, and J. E. García-Ramos, *Phys. Rev. A* **80**, 032111 (2009).
- [56] P. Pérez-Fernández, P. Cejnar, J. M. Arias, J. Dukelsky, J. E. García-Ramos, and A. Relaño, *Phys. Rev. A* **83**, 033802 (2011).
- [57] G. Engelhardt, V. M. Bastidas, W. Kopylov, and T. Brandes, *Phys. Rev. A* **91**, 013631 (2015).
- [58] L. F. Santos and F. Pérez-Bernal, *Phys. Rev. A* **92**, 050101(R) (2015).
- [59] L. F. Santos, M. Távora, and F. Pérez-Bernal, *Phys. Rev. A* **94**, 012113 (2016).
- [60] F. Pérez-Bernal and L. F. Santos, *Fortschr. Phys.* **65**, 1600035 (2017).
- [61] M. Kloc, P. Stránský, and P. Cejnar, *Phys. Rev. A* **98**, 013836 (2018).
- [62] Q. Wang and F. Pérez-Bernal, *Phys. Rev. A* **100**, 022118 (2019).
- [63] S. Pilatowsky-Cameo, J. Chávez-Carlos, M. A. Bastarrachea-Magnani, P. Stránský, S. Lerma-Hernández, L. F. Santos, and J. G. Hirsch, *Phys. Rev. E* **101**, 010202(R) (2020).
- [64] Q. Wang and F. Pérez-Bernal, *Phys. Rev. E* **103**, 032109 (2021).
- [65] R. Puebla, A. Relaño, and J. Retamosa, *Phys. Rev. A* **87**, 023819 (2013).
- [66] R. Puebla and A. Relaño, *Europhys. Lett.* **104**, 50007 (2013).
- [67] Q. Wang and H. T. Quan, *Phys. Rev. E* **96**, 032142 (2017).
- [68] Q. Wang and F. Pérez-Bernal, *Phys. Rev. A* **100**, 062113 (2019).
- [69] A. Polkovnikov, K. Sengupta, A. Silva, and M. Vengalattore, *Rev. Mod. Phys.* **83**, 863 (2011).
- [70] P. Pérez-Fernández, A. Relaño, J. M. Arias, P. Cejnar, J. Dukelsky, and J. E. García-Ramos, *Phys. Rev. E* **83**, 046208 (2011).
- [71] C. M. Lóbez and A. Relaño, *Phys. Rev. E* **94**, 012140 (2016).
- [72] M. A. Bastarrachea-Magnani, S. Lerma-Hernández, and J. G. Hirsch, *J. Stat. Mech. Theory Exp.* (2016) 093105.
- [73] P. Pérez-Fernández and A. Relaño, *Phys. Rev. E* **96**, 012121 (2017).
- [74] M. Šindelka, L. F. Santos, and N. Moiseyev, *Phys. Rev. A* **95**, 010103(R) (2017).
- [75] P. Cejnar, P. Stránský, M. Macek, and M. Kloc, *J. Phys. A: Math. Theor.* **54**, 133001 (2021).
- [76] A. Sugita, *J. Phys. A: Math. General* **36**, 9081 (2003).
- [77] K. Furuya, M. de Aguiar, C. Lewenkopf, and M. Nemes, *Ann. Phys.* **216**, 313 (1992).
- [78] W.-M. Zhang, D. H. Feng, and R. Gilmore, *Rev. Mod. Phys.* **62**, 867 (1990).
- [79] J.-P. Gazeau, *Coherent States in Quantum Physics* (Wiley, Weinheim, 2009).
- [80] M. de Aguiar, K. Furuya, C. Lewenkopf, and M. Nemes, *Ann. Phys.* **216**, 291 (1992).
- [81] A. Sugita and H. Aiba, *Phys. Rev. E* **65**, 036205 (2002).
- [82] F. Mintert and K. Życzkowski, *Phys. Rev. A* **69**, 022317 (2004).
- [83] A. Wehrl, *Rep. Math. Phys.* **16**, 353 (1979).
- [84] E. H. Lieb, in *Inequalities* (Springer, Berlin, 2002), pp. 359–365.
- [85] S. Gnutzmann and K. Życzkowski, *J. Phys. A: Math. Gen.* **34**, 10123 (2001).
- [86] D. Villaseñor, S. Pilatowsky-Cameo, M. A. Bastarrachea-Magnani, S. Lerma-Hernández, and J. G. Hirsch, *Phys. Rev. E* **103**, 052214 (2021).
- [87] I. Varga and J. Pipek, *Phys. Rev. E* **68**, 026202 (2003).
- [88] H. Lipkin, N. Meshkov, and A. Glick, *Nucl. Phys.* **62**, 188 (1965).
- [89] P. Ribeiro, J. Vidal, and R. Mosseri, *Phys. Rev. E* **78**, 021106 (2008).
- [90] G. Engelhardt, V. M. Bastidas, C. Emary, and T. Brandes, *Phys. Rev. E* **87**, 052110 (2013).
- [91] R. Botet and R. Jullien, *Phys. Rev. B* **28**, 3955 (1983).
- [92] S. Dusuel and J. Vidal, *Phys. Rev. B* **71**, 224420 (2005).
- [93] O. Castaños, R. López-Peña, J. G. Hirsch, and E. López-Moreno, *Phys. Rev. B* **74**, 104118 (2006).
- [94] S. Campbell, *Phys. Rev. B* **94**, 184403 (2016).
- [95] J. Bao, B. Guo, H.-G. Cheng, M. Zhou, J. Fu, Y.-C. Deng, and Z.-Y. Sun, *Phys. Rev. A* **101**, 012110 (2020).
- [96] A. C. Lourenço, S. Calegari, T. O. Maciel, T. Debarba, G. T. Landi, and E. I. Duzzioni, *Phys. Rev. B* **101**, 054431 (2020).
- [97] A. Russomanno, F. Iemini, M. Dalmonte, and R. Fazio, *Phys. Rev. B* **95**, 214307 (2017).
- [98] Y. Huang, T. Li, and Z.-q. Yin, *Phys. Rev. A* **97**, 012115 (2018).
- [99] S. Morrison and A. S. Parkins, *Phys. Rev. Lett.* **100**, 040403 (2008).
- [100] T. Zibold, E. Nicklas, C. Gross, and M. K. Oberthaler, *Phys. Rev. Lett.* **105**, 204101 (2010).
- [101] A. G. Araujo-Ferreira, R. Auccaise, R. S. Sarthour, I. S. Oliveira, T. J. Bonagamba, and I. Roditi, *Phys. Rev. A* **87**, 053605 (2013).
- [102] P. Jurcevic, H. Shen, P. Hauke, C. Maier, T. Brydges, C. Hempel, B. P. Lanyon, M. Heyl, R. Blatt, and C. F. Roos, *Phys. Rev. Lett.* **119**, 080501 (2017).
- [103] V. Makhalov, T. Satoor, A. Evrard, T. Chalopin, R. Lopes, and S. Nascimbene, *Phys. Rev. Lett.* **123**, 120601 (2019).
- [104] J. A. Muniz, D. Barberena, R. J. Lewis-Swan, D. J. Young, J. R. K. Cline, A. M. Rey, and J. K. Thompson, *Nature (London)* **580**, 602 (2020).
- [105] J. I. Latorre, R. Orús, E. Rico, and J. Vidal, *Phys. Rev. A* **71**, 064101 (2005).
- [106] P. Titum and M. F. Maghrebi, *Phys. Rev. Lett.* **125**, 040602 (2020).
- [107] M. Feingold and A. Peres, *Physica D* **9**, 433 (1983).
- [108] M. Feingold, N. Moiseyev, and A. Peres, *Phys. Rev. A* **30**, 509 (1984).
- [109] A. P. Hines, R. H. McKenzie, and G. J. Milburn, *Phys. Rev. A* **71**, 042303 (2005).
- [110] Y. Fan, S. Gnutzmann, and Y. Liang, *Phys. Rev. E* **96**, 062207 (2017).
- [111] D. Mondal, S. Sinha, and S. Sinha, *Phys. Rev. E* **102**, 020101(R) (2020).
- [112] D. T. Robb and L. E. Reichl, *Phys. Rev. E* **57**, 2458 (1998).
- [113] S. Ray, S. Sinha, and D. Sen, *Phys. Rev. E* **100**, 052129 (2019).
- [114] V. Dodonov, I. Malkin, and V. Man'ko, *Physica* **72**, 597 (1974).
- [115] R. N. P. Maia, F. Nicacio, R. O. Vallejos, and F. Toscano, *Phys. Rev. Lett.* **100**, 184102 (2008).
- [116] C. Eichler, D. Bozyigit, C. Lang, L. Steffen, J. Fink, and A. Wallraff, *Phys. Rev. Lett.* **106**, 220503 (2011).

- [117] G. Kirchmair, B. Vlastakis, Z. Leghtas, S. E. Nigg, H. Paik, E. Ginossar, M. Mirrahimi, L. Frunzio, S. M. Girvin, R. J. Schoelkopf *et al.*, [Nature \(London\) \*\*495\*\*, 205 \(2013\)](#).
- [118] J. G. Bohnet, B. C. Sawyer, J. W. Britton, M. L. Wall, A. M. Rey, M. Foss-Feig, and J. J. Bollinger, [Science \*\*352\*\*, 1297 \(2016\)](#).
- [119] F. Bouchard, P. de la Hoz, G. Björk, R. W. Boyd, M. Grassl, Z. Hradil, E. Karimi, A. B. Klimov, G. Leuchs, J. Řeháček, and L. L. Sánchez-Soto, [Optica \*\*4\*\*, 1429 \(2017\)](#).
- [120] H. Strobel, W. Muessel, D. Linnemann, T. Zibold, D. B. Hume, L. Pezzè, A. Smerzi, and M. K. Oberthaler, [Science \*\*345\*\*, 424 \(2014\)](#).